Nano Research

ISSN 1998-0124 CN 11-5974/O4
https://doi.org/10.26599/NR.2026.94909274

Research Article

Ag-glued Au/C catalyst layer for durable CO_2-to-CO electrolysis at industrial current density

Siyang Wang, Xueqin Wu, Wenrong Yang, Qianqian Ren, Abrar Amna, Shi Hu(✉)
Department of Chemistry, School of Science, Tianjin Key Laboratory of Molecular Optoelectronic Science, Tianjin University, Tianjin 300072, China

Nano Res., **Just Accepted Manuscript** • https://doi.org/10.26599/NR.2026.94909274
https://www.sciopen.com/journal/1998-0124 on Oct. 20, 2026

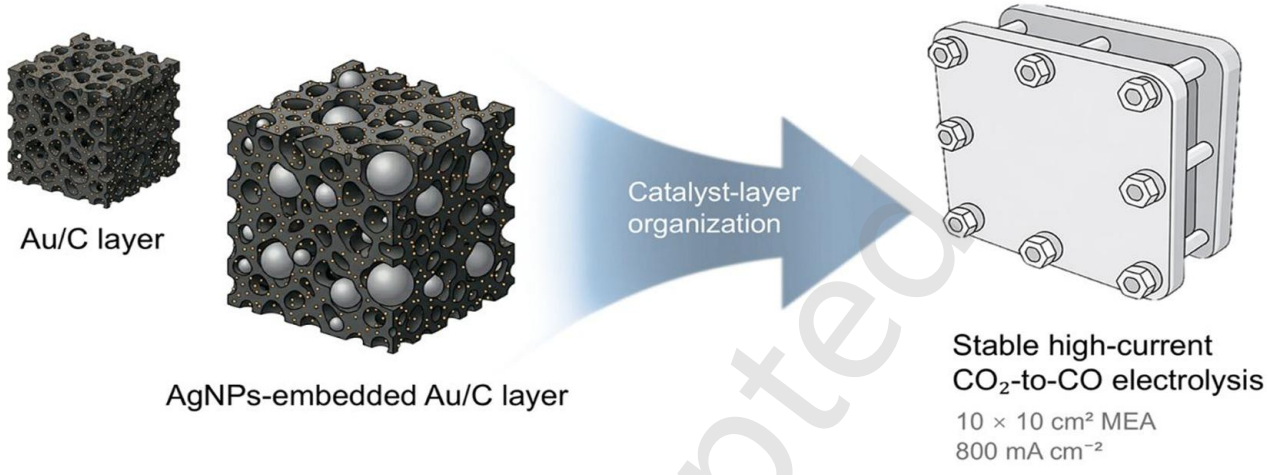
© The Authors(s)

Just Accepted

This is a "Just Accepted" manuscript, which has been examined by the peer-review process and has been accepted for publication. A "Just Accepted" manuscript is published online shortly after its acceptance,which is prior to technical editing and formatting and author proofing. Tsinghua University Press (TUP) provides "Just Accepted" as an optional and free service which allows authors to make their results available to the research community as soon as possible after acceptance. After a manuscript has been technically edited and formatted, and the page proofs have been corrected, it will be removed from the "Just Accepted" web site and published officially with volume and article number (e.g., *Nano Research*, **2025**, *18*, 94906990). Please note that technical editing may introduce minor changes to the manuscript text and/or graphics which may affect the content, and all legal disclaimers that apply to the journal pertain. In no event shall TUP be held responsible for errors or consequences arising from the use of any information contained in these "Just Accepted" manuscripts. To cite this anuscript please use its Digital Object Identifier (DOI®),which is identical for all formats of publication.

Just Accepted

Insert Table of Contents artwork here



We report an Ag-glued Au/C catalyst layer in which large Ag nanoparticles are physically embedded in a nano-Au/C matrix. In a 10 cm × 10 cm zero-gap electrolyzer at 800 mA cm^{-2}, this catalyst layer sustains stable CO_2-to-CO electrolysis over 200 h, showing that catalyst-layer organization, beyond composition, is a practical design lever.

Just Accepted

Nano Research

Open Access

Research Article

Ag-glued Au/C catalyst layer for durable CO_2-to-CO electrolysis at industrial current density

Siyang Wang, Xueqin Wu, Wenrong Yang, Qianqian Ren, Abrar Amna, and Shi Hu

Department of Chemistry, School of Science, Tianjin Key Laboratory of Molecular Optoelectronic Science, Tianjin University, Tianjin 300072, China

Received: 2 May 2026; **Revised:** 24 September 2026; **Accepted:** 20 October 2026

Address correspondence to rychushi@gmail.com

Cite this article: *Nano Research*, 2026, 19, 94909274 https://doi.org/10.26599/NR.2026.94909274

ABSTRACT: Durable CO_2-to-CO electrolysis at industrial current density remains a key bottleneck in low-temperature systems, especially in zero-gap electrolyzers, where prolonged high-rate operation drives impedance growth and destabilizes the catalyst-layer reaction environment. Here, we report an Ag-glued Au/C catalyst layer, in which large Ag nanoparticles are physically embedded in a nano-Au/C matrix. In a 10 cm × 10 cm zero-gap electrolyzer at 800 mA cm^{-2}, Ag-glued Au/C (7:3) operated continuously for 200 h and degraded substantially more slowly than nano-Au/C, with cell-voltage and CO Faradaic-efficiency (FE_{CO}) decay rates of 1.3 mV h^{-1} and 0.12% h^{-1}, respectively, and slower impedance growth. In flow cell tests, it reached 92.9% FE_{CO} at 139 mA cm^{-2}. Neither AuAg alloying nor nanoscale Au/C-Ag/C mixing replicated this durability at the same composition, pointing to a catalyst-layer-organization effect that slows impedance growth under sustained operation. Within the configurations examined here, these results indicate that catalyst-layer organization, beyond composition, offers a practical design lever for durable CO_2-to-CO electrolysis under industrially relevant zero-gap operation.

KEYWORDS: CO_2-to-CO electrolysis, zero-gap electrolyzer, catalyst-layer architecture, industrial current density

1 Introduction

The growing deployment of renewable electricity is driving demand for electrified chemistry that can absorb intermittent power and help close the carbon cycle. Electrochemical CO_2 reduction provides a direct pathway from CO_2 to value-added chemicals and fuels using renewable electrons, and among accessible products, carbon monoxide is one of the most practical targets in low-temperature CO_2 electrolysis [1]. As a two-electron product, CO combines simple reaction chemistry with strong downstream utility as a commodity gas and as a key syngas component. Techno-economic analyses likewise identify CO among the most competitive near-term products, provided that electrolysis can be sustained at sufficiently high rates, high efficiencies, and adequate durability [2]. This positions durable CO_2-to-CO electrolysis at industrial current density at the center of practical electrolyzer development [3]. Zero-gap electrolyzers have emerged as the configuration of choice for pushing CO_2 electrolysis toward such regimes, offering a scalable route to high-rate conversion beyond conventional liquid-electrolyte cells [4, 5]. Yet sustained operation at large current densities remains difficult, as high-rate conversion makes it hard to retain CO selectivity and cell stability over time [6, 7]. Under these conditions, the catalyst layer becomes a confined reaction environment in which CO_2 access, ionic conduction, and liquid accumulation evolve together during operation [8], making catalyst-layer organization especially consequential for transport-coupled performance.

Au-based catalysts are widely recognized for selective CO production, particularly in systems targeting high CO partial current density [9-11]. Studies on Au–Ag catalysts have largely been framed around alloying, electronic interaction, and composition optimization, with performance differences commonly interpreted through an active-site-centered picture [12-14]. While valuable, such frameworks do not address a different question that becomes especially relevant under high-current operation in zero-gap electrolyzers: whether physically embedding a secondary phase into a nano-Au/C catalyst layer can create a configuration that supports more durable CO_2-to-CO electrolysis, even at comparable Au/Ag composition. Related work on three-phase interfaces, hydrophobic micro-environments, and ionomer-regulated catalyst layers suggests that catalyst-layer organization can reshape performance beyond what composition alone prescribes [15-19]. Here we report an Ag-glued Au/C catalyst layer, in which large Ag nanoparticles are physically embedded in a nano-Au/C matrix (Ag-glued Au/C), and evaluate it from fixed-composition flow cell comparisons to a zero-gap electrolyzer operated at 800 mA cm^{-2} [20-22]. Whether this configuration may support transport and active site utilization in ways that differ from a single nano-Au/C layer is a hypothesis examined here, with detailed mechanistic analysis deferred to later sections.

Here, we constructed an Ag-glued Au/C catalyst layer by physically embedding large Ag nanoparticles in a nano-Au/C matrix. Ag-glued Au/C was prepared by direct physical mixing of Au/C with commercial Ag nanoparticles, and Ag-glued Au/C (7:3) is used as the representative sample throughout the

Just Accepted

structural analysis below. For the fixed-composition electrochemical contrast that follows, AuAg alloy/C (7:3) and Au/C + Ag/C (7:3) were independently prepared as an alloy-type reference and a carbon-supported physically mixed reference, respectively.

2 Experimental

Au/C was synthesized by colloidal reduction of Au precursors followed by supporting on carbon black, giving a nominal metal loading of 50 wt%. Ag-glued Au/C catalysts were prepared by physically mixing Au/C with commercial Ag nanoparticles at the desired Au:Ag atomic ratio, followed by grinding. Additional carbon black was introduced when necessary to maintain a comparable total metal loading among samples. AuAg alloy/C was synthesized by slow-heating co-reduction of Au and Ag precursors in an organic medium, followed by carbon supporting. Au/C + Ag/C was prepared by physically mixing the corresponding carbon-supported components. Detailed synthesis procedures are provided in the Supporting Information. Catalyst inks were prepared in ethanol/water (9:1, v/v) with a solids concentration of 10 mg mL^{-1}, with Nafion solution as the ionomer binder. After alternating magnetic stirring and ultrasonication, the inks were spray-coated to prepare the gas diffusion electrode

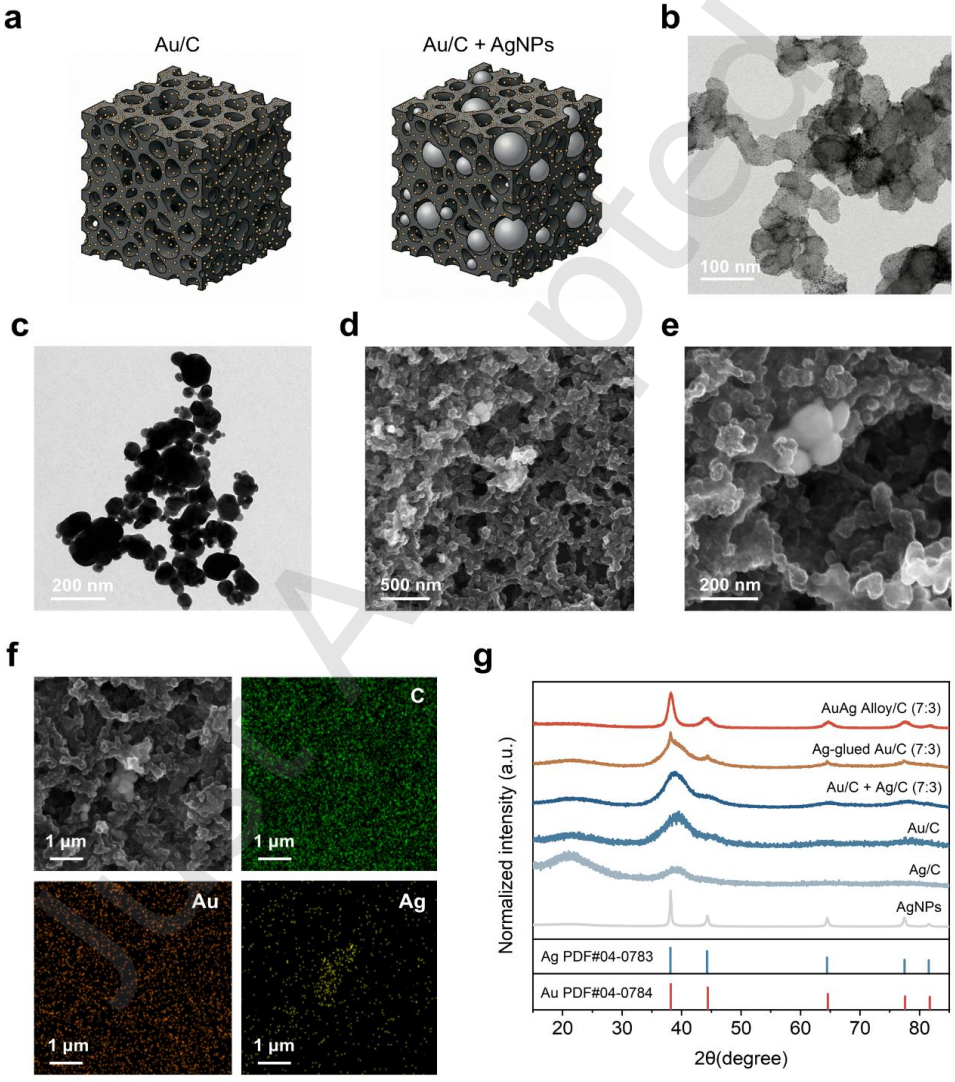


Figure 1. Catalyst-layer design and structural features of the Ag-glued Au/C catalyst. (a) Schematic illustration of the catalyst-layer organization of Au/C and Ag-glued Au/C. (b) TEM image of Au/C. (c) TEM image of AgNPs. (d) Surface SEM image of the Ag-glued Au/C catalyst layer on carbon paper. (e) Higher-magnification SEM image of the Ag-glued Au/C catalyst layer, showing AgNPs physically embedded in the Au/C matrix. (f) SEM image and corresponding elemental maps of C, Au, and Ag for the Ag-glued Au/C catalyst layer. (g) XRD patterns of Au/C, AgNPs, Ag-glued Au/C (7:3), and AuAg alloy/C (7:3). At the same nominal Au:Ag ratio, Ag-glued Au/C organizes the Au and Ag phases differently from both the alloy-type and the conventionally mixed nanoscale references, which sets up the question pursued below: whether catalyst-layer organization, at fixed overall composition, is associated with the electrochemical and durability behavior.

For flow-cell measurements, the inks were deposited on carbon paper, yielding a total cathode metal loading of ca. 0.5 mg cm^{-2}. For zero-gap electrolyzer tests, membrane electrode assemblies (MEAs) were prepared by forming Au/C or Ag-glued Au/C (7:3)

cathode catalyst layers on commercial anode-coated membranes using the same fabrication protocol. Detailed electrode-fabrication procedures and electrochemical operating parameters, including the membrane type, ionomer type and content, CO_2 flow rate, anolyte flow rate, gas humidification condition, and operating temperature for both flow-cell and zero-gap electrolyzer tests, are provided in Text S2–S4 in the Supporting Information. The flow-cell setup and exploded-view configuration are shown in Figs. S6 and S7.

3 Results and discussion

3.1 Catalyst-layer design

The catalyst-layer design and the reference architectures are schematically summarized in Fig. 1a. Transmission electron microscopy (TEM) shows that the Au phase in Au/C consists of uniformly dispersed nanoscale particles anchored on carbon black, with a mean size in the ca. 3–5 nm range (Fig. 1b and Fig. S1). The commercial Ag phase, in contrast, exhibits a much broader particle-size distribution in the tens-to-low hundreds of nanometers (Fig. 1c and Fig. S2). When the two are combined, the deposited Ag-glued Au/C (7:3) electrode forms a continuous porous coating on the carbon-paper substrate (Fig. 1d), within which large Ag particles (tens to low hundreds of nanometers) are visible as discrete bright domains interspersed in the finer nano-Au/C matrix (Fig. 1e), providing direct visual evidence of the size-contrast-based embedded organization. Top-view elemental mapping shows broadly distributed Au together with spatially discrete Ag-rich regions within the same catalyst-layer area (Fig. 1f), and cross-sectional scanning electron microscopy–energy-dispersive X-ray spectroscopy (SEM-EDS) mapping further indicates that Ag is distributed across the catalyst-layer thickness rather than being confined to the outermost surface (Fig. S3). Collectively, these microscopy and mapping results indicate a structurally distinct organization of the Au and Ag phases within the Ag-glued Au/C catalyst layer compared with the references introduced above.

X-ray diffraction (XRD) provides complementary phase-level information. Au/C displays broadened diffraction features characteristic of small supported metal nanoparticles, whereas the commercial Ag nanoparticles show sharper reflections consistent with their larger crystalline domains. Ag-glued Au/C (7:3) retains the diffraction signatures of both constituent phases, while AuAg alloy/C (7:3) exhibits a distinct profile consistent with alloy formation (Fig. 1g). We note that AuAg alloy/C also has a somewhat larger mean particle size (ca. 10–13 nm; Figs. S11 and S12) than the nano-Au/C building blocks of the physically mixed references (ca. 3–5 nm; Fig. S1). It is therefore treated in this work as an alloy-type reference in the fixed-composition contrast rather than as a strictly size-matched control.

3.2 Composition and surface state

Before turning to the electrochemical comparison, we verified that the three 7:3 catalysts—Ag-glued Au/C (7:3), AuAg alloy/C (7:3), and Au/C + Ag/C (7:3)—were comparable in overall loading and bulk Au/Ag composition. Thermogravimetric analysis (TGA) was used here not to probe catalyst-layer organization, but to verify that the three 7:3 catalysts are comparable in total metal content. Residual masses at 800 °C fall within a narrow range across all samples (40–45 wt%; Fig. 2a and Table S1), confirming that differences in electrochemical performance observed later cannot be attributed to systematic variations in metal loading, with representative full TGA curves provided in Fig. S4. Inductively coupled plasma optical emission spectroscopy (ICP-OES) further indicates that the measured Au/Ag ratios remain close to the intended values across the catalyst series (Fig. 2b and Table S2). For the three 7:3 catalysts entering the fixed-composition contrast, the measured Ag fractions are close to one another, establishing the compositional basis on which the subsequent electrochemical divergence is interpreted.

X-ray photoelectron spectroscopy (XPS) was then used to examine whether the three 7:3 catalysts differ markedly in surface chemical state. Survey spectra show the expected C 1s, O 1s, Au 4f, and Ag 3d features consistent with the designed compositions (Fig. S5). In the high-resolution Au 4f spectra, all three catalysts display the characteristic Au doublet, while AuAg alloy/C (7:3) shows a more evident spectral shift than the two physically mixed samples (Fig. 2c). A similar tendency is observed in the Ag 3dregion (Fig. 2d), where the alloy reference again exhibits the more pronounced shift, whereas Ag-glued Au/C (7:3) and Au/C + Ag/C (7:3) remain much closer to one another. The summarized binding-energy values (Fig. 2e) are consistent with this pattern: the more noticeable surface-state differences in the present set are associated with the alloy reference, while the two physically mixed catalysts fall within a comparable range at the resolution of this analysis. The XPS differences between Ag-glued Au/C (7:3) and Au/C + Ag/C (7:3) in particular are limited, so the electrochemical divergence observed below is not readily attributed to composition mismatch or to a dominant surface-state difference alone; at the same time, the present data do not exclude electronic contributions outright, but rather constrain how strongly such contributions can be invoked on the basis of the current evidence. The binding energies, fit uncertainties, full widths at half maximum (FWHM) values, and spin-orbit splitting parameters are compiled in Table S3.

3.3 Composition and organization effects

To separate composition-level effects from those associated with how Au and Ag are arranged in the catalyst layer, we adopted a two-step analysis in the flow cell configuration [23, 24]. In the first step, a physically mixed Au/C–Ag series spanning 10:0 to 0:10 Au:Ag ratios was used to identify a suitable composition window. In the second step, we fixed the overall Au:Ag ratio and contrasted three catalysts with distinct Au/Ag arrangements. Fig. 3 therefore establishes the compositional basis for the fixed-composition contrast in Fig. 4, rather than serving as the main electrochemical claim of this section.

Within the physically mixed series, changing the Au:Ag ratio systematically altered the electrochemical response (Fig. 3a–d). Pure Au/C (the 10:0 endpoint) retained the highest CO Faradaic efficiency (FE_{CO}) but only a moderate CO partial current density (j_{CO}); increasing the Ag fraction raised the total current response (Fig. 3a) while lowering CO selectivity, so that j_{CO} peaked at the intermediate Au: Ag = 7:3 composition before decreasing toward the Ag-rich end (Fig. 3c and Table S4). Among the tested compositions, Au: Ag = 7:3 provided the most suitable window for the subsequent contrast, because it retained CO selectivity close to that of Au/C while delivering a higher CO partial current density. Compositions with larger Ag fractions were less

Just Accepted

suitable here, as the increased current response was accompanied by reduced CO selectivity. Corresponding H_2 Faradaic efficiency (FE_{H2}) and H_2 partial current density (j_{H2}) data for this series are provided in Figs. S8 and S9. In this sense, Au: Ag = 7:3 is not advanced here as a universal optimum across Au–Ag CO_2 reduction reaction (CO_2RR) catalysts, but as the composition at which the organization question can be examined most cleanly. Across the physically mixed series (10:0, 7:3, 5:5, 3:7, and 0:10), the 7:3 composition gave the most favorable CO_2-to-CO response within the screened window, with performance decreasing toward both the Au-rich (10:0) and Ag-rich (3:7, 0:10) ends (Fig. 3a–d and Figs. S8–S9)

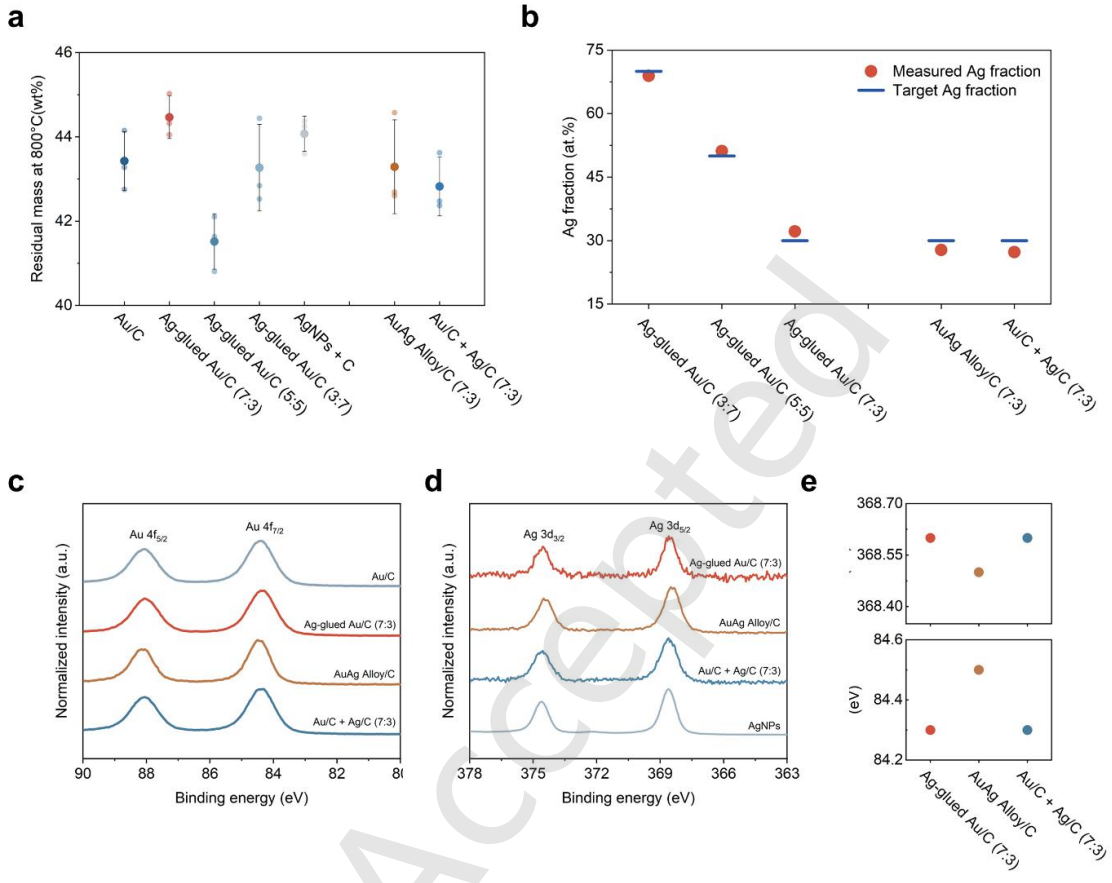


Figure 2. Composition and surface chemical states of the catalysts. (a) Residual mass ratios of the catalyst samples determined by TGA. (b) Au and Ag compositions of the catalyst samples determined by ICP-OES. (c) Au 4f XPS spectra of Ag-glued Au/C (7:3), AuAg alloy/C (7:3), and Au/C + Ag/C (7:3). (d) Ag 3d XPS spectra of the same three samples. (e) Summary of the XPS-derived Au 4f and Ag 3d binding energies.

This first step, however, does not by itself isolate the role of catalyst-layer organization. Varying the Au:Ag ratio simultaneously alters the amount of the large Ag phase introduced into the nano-Au/C matrix and, consequently, the resulting catalyst-layer arrangement composition. A fixed-composition contrast is therefore needed to examine whether, at the same overall Au:Ag ratio, different Au/Ag arrangements yield distinguishable electrochemical behavior. We fixed the overall Au:Ag ratio at 7:3 and contrasted three catalysts with distinct Au/Ag arrangements: Ag-glued Au/C (7:3), AuAg alloy/C (7:3), and Au/C + Ag/C (7:3). This is the central electrochemical contrast of the present study.

As shown in Fig. 4a, Ag-glued Au/C (7:3) exhibited the largest cathodic current response across the investigated potential range. Product analysis revealed a pronounced divergence at fixed composition: Ag-glued Au/C (7:3) sustained the highest FE_{CO} and j_{CO} throughout the measured potential window (Fig. 4b,c). At −1.37 V vs. reversible hydrogen electrode (RHE), it delivered an FE_{CO} of 92.9% at a j_{CO} of 139.1 mA cm^{-2}, contrasted with 79.1% and 69.7 mA cm^{-2} for AuAg alloy/C (7:3) and 85.7% and 97.0 mA cm^{-2} for Au/C + Ag/C (7:3). The H_2 partial current density followed the opposite trend, with Ag-glued Au/C (7:3) showing the lowest j_{H2} among the three catalysts (Fig. 4d), and the corresponding FE_{H2} data are provided in Fig. S10.

The AuAg alloy/C (7:3) reference has a somewhat larger particle size than the physically mixed catalysts and is therefore used as an alloy-type reference rather than as an ideal organization-only control. Even with this caveat in mind, neither alloying Au and Ag into a single phase nor combining Au/C with Ag/C at the same overall composition reproduced the FE_{CO}–j_{CO} behavior of Ag-glued Au/C (7:3). Read against the compositional comparability and the limited surface-state differences noted above, this indicates that composition alone does not account for the observed divergence among these references, although a mechanistic reading of the divergence is left to the discussion below (Text S7); the three 7:3 electrodes also show comparable catalyst-layer thickness, ionomer-to-carbon ratio, and surface morphology (Fig. S18 and Text S8).

Just Accepted

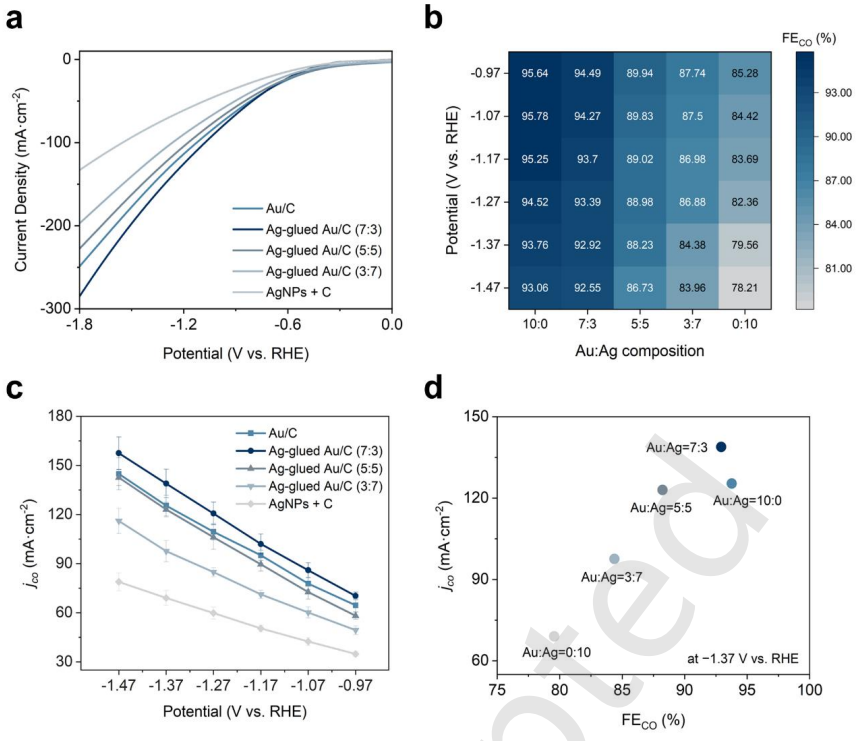


Figure 3. Composition-dependent CO_2-to-CO electrolysis performance of the Ag-glued Au/C series in a flow cell. (a) Linear sweep voltammetry curves of Ag-glued Au/C catalysts with Au:Ag ratios of 10:0, 7:3, 5:5, 3:7, and 0:10. (b) Heat map of FE_{CO} at different applied potentials. (c) CO partial current density (j_{CO}) as a function of applied potential. (d) FE_{CO} versus j_{CO} at −1.37 V vs. RHE.

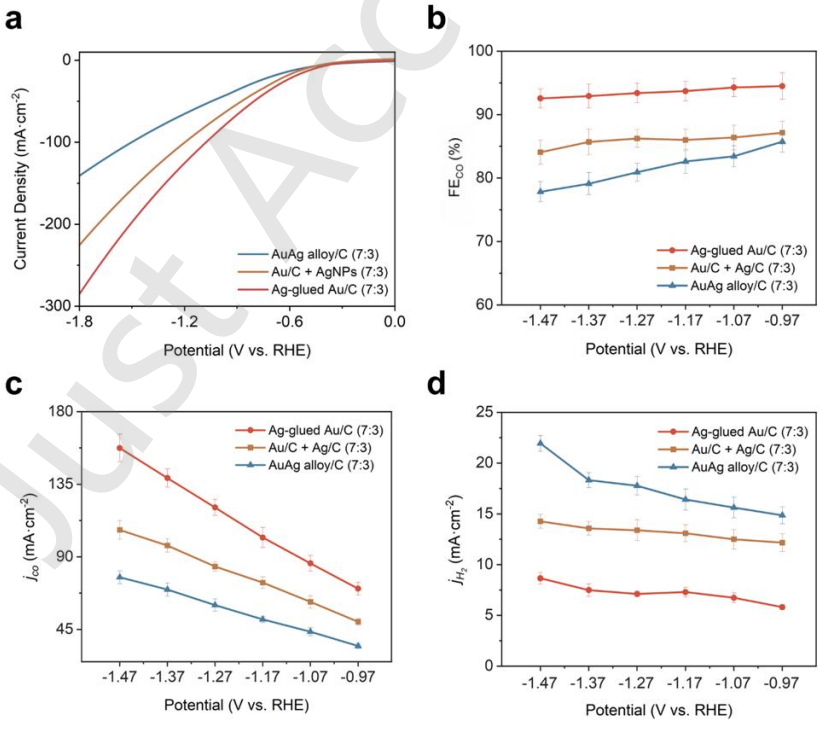


Figure 4. Organization-dependent CO_2-to-CO electrolysis performance at a fixed Au:Ag ratio of 7:3 in a flow cell. (a) Linear sweep voltammetry curves of Ag-glued Au/C (7:3), AuAg alloy/C (7:3), and Au/C + Ag/C (7:3). (b) FE_{CO} at different applied potentials. (c) CO partial current density (j_{CO}) at different applied potentials. (d) H_2 partial current density (jH_2) at different applied potentials.

Quantifying this contrast on a per-metal basis reinforces the same conclusion. Because all electrodes were prepared at an identical total metal loading of 0.5 mg cm^{-2}, the partial CO current densities (j_{CO}) at −1.37 V vs. RHE can be directly converted to metal-mass activities, which removes loading as a variable and isolates the effect of catalyst-layer organization. On this basis, Ag-glued Au/C (7:3) delivers a metal-mass activity of 278.1 mA mg^{-1}, higher than the physically mixed Au/C + Ag/C

Just Accepted

(193.9 mA mg^{-1}) and the AuAg alloy/C (139.5 mA mg^{-1}) of the same nominal composition (Table S4). Since the metal content is fixed, these differences are not attributable to the amount of metal and instead indicate differences in effective active-site utilization, consistent with an organization-governed local transport environment rather than an intrinsic composition effect. A complementary electrochemically active surface area (ECSA)-resolved and operando analysis that separately quantifies intrinsic per-site activity and effective site utilization is identified as a direction for future work (Text S6).

3.4 Engineering-scale validation

We next examined whether the performance advantage identified above for Ag-glued Au/C would remain evident under engineering-relevant operation [25, 26]. To this end, Au/C and Ag-glued Au/C (7:3) were evaluated in a 10 cm × 10 cm zero-gap electrolyzer under galvanostatic operation at 80 A, corresponding to 800 mA cm^{-2}. Photographs of the assembled cell and its installation on the test bench are shown in Fig. 5a–c. The test configuration is illustrated in Figs. S14 and S15, and the detailed operating conditions, including membrane type, ionomer type and content, CO_2 flow rate, anolyte flow rate, humidification condition, and operating temperature, are provided in Text S4.

The initial impedance response of the two electrodes was closely comparable [27, 28]. At 1 h after startup, the Nyquist spectra of Au/C and Ag-glued Au/C (7:3) nearly overlapped (Fig. 5d), with area resistances of 0.58 Ω cm^2 and 0.57 Ω cm^2, respectively. After 60 h of continuous operation, however, a clear divergence had developed between the two large-area electrodes (Fig. 5e): the impedance arc of Au/C expanded substantially and its area resistance rose to 0.78 Ω cm^2, whereas Ag-glued Au/C (7:3) retained a smaller arc with an area resistance of 0.65 Ω cm^2. The corresponding distribution of relaxation times (DRT) profiles at 60 h (Fig. 5f) show weaker features for Ag-glued Au/C (7:3) across the measured frequency range of 0.01 Hz to 100 kHz. A feature in the 1–10 Hz region, commonly associated with mass-transport-related processes, is more pronounced for Au/C than for Ag-glued Au/C (7:3), suggesting that the two catalyst layers differ in how they accommodate mass transport during sustained high-current operation. Rather than interpreting the DRT peaks in terms of any specific individual process here, we read the overall impedance evolution as a time-evolving operational feature: the 1 h → 60 h progression indicates that the resistance difference between Au/C and Ag-glued Au/C (7:3) develops during sustained high-current operation, pointing to a difference in how the two catalyst layers accommodate that operation over time rather than to a disparity in the initial state.

This impedance-level divergence is reflected directly in the long-term electrolysis behavior [29]. Under continuous operation at 800 mA cm^{-2}, Au/C showed a voltage decay rate of 4.8 mV h^{-1}, whereas Ag-glued Au/C (7:3) exhibited a markedly lower rate of 1.3 mV h^{-1} (Fig. 5g). During the first ~10 h, both electrodes showed an initial decrease and subsequent recovery of cell voltage before settling into their respective long-term trends. This early feature coincided with the stepwise current ramp used at startup (30 A and 60 A for 3 h each before reaching 80 A) and is likely associated with conventional break-in processes, including progressive membrane and catalyst-layer wetting, activation of the electrode–electrolyte interface, and redistribution of ions and water within the catalyst layer as steady-state operation is established. Because this behavior was common to all electrodes rather than specific to Au/C, we attribute it to the cell break-in stage rather than to early degradation, and the divergence between Au/C and Ag-glued Au/C (7:3) developed only during the subsequent sustained operation. The Au/C cell voltage rose progressively and then accelerated upward once it exceeded 4.0 V, reaching the failure threshold at around 86 h. In contrast, Ag-glued Au/C (7:3) did not reach the failure threshold over the same period and was operated continuously for 200 h under the same conditions. CO-selectivity retention followed the same trend (Fig. 5h): the FE_{CO} decay rate decreased from 0.255% h^{-1} for Au/C to 0.122% h^{-1} for Ag-glued Au/C (7:3), and the latter maintained substantially higher FE_{CO} throughout the prolonged run. The corresponding FE_{H2} evolution is provided in Fig. S16. Across the 10 cm × 10 cm zero-gap contrast, the advantage of Ag-glued Au/C (7:3) over Au/C seen in the flow cell contrast persists under engineering-relevant operation, with slower resistance growth, improved voltage stability, and better CO-selectivity retention during sustained operation at 800 mA cm^{-2}. Because this contrast was conducted between Au/C and Ag-glued Au/C (7:3) rather than across all three fixed-composition arrangements, it serves as cross-scale validation of the Ag-glued Au/C (7:3) arrangement identified in the flow cell contrast rather than as an independent fixed-composition proof.

The CO_2 single-pass utilization (SPU) of the Ag-glued Au/C (7:3) zero-gap electrolyzer was 44.6% at the beginning of the 200 h test (FE_{CO} = 96%, V_{cell} = 3.20 V) and decreased to 29.3% at ~200 h (FE_{CO} = 63%, V_{cell} = 3.45 V). The corresponding CO energy efficiency (EE_CO) was 40.0% initially and 24.3% after ~200 h operation. Full calculation details are provided in Supporting Information.

Beyond this organization-level contrast, the long-term operation also provides information on the practical stability of the electrolyte environment. In the present zero-gap configuration, a cation-exchange membrane was used together with a recirculated 0.5 M $KHCO_3$ anolyte, which provided ionic conductivity and pH buffering on the anode side. Because the membrane preferentially conducts cations, K^+ migration toward the cathode is expected during operation, while direct anion crossover from the anolyte is suppressed. Under these conditions, carbonate-related accumulation is more likely to affect the cathode-side reaction environment than to cause rapid depletion of the recirculated anolyte. The relatively large anolyte reservoir and continuous recirculation further help moderate concentration and pH changes during the test. During the 200 h operation at 800 mA cm^{-2}, no obvious change in the anolyte, salt precipitation, or flow-channel blockage was observed, consistent with the stable voltage and FE_{CO} profiles in Fig. 5g, h. These observations indicate that carbonate management did not cause abrupt failure over the tested duration, although a contribution of cathode-side accumulation to the gradual FE_{CO} decline cannot be excluded. Nevertheless, cathode-side (bi)carbonate accumulation and gradual cation redistribution may become more consequential during substantially longer operation, where periodic electrolyte replenishment and optimized water management may further improve long-term electrolyte stability. Control electrodes with the same nominal Au:Ag composition

Just Accepted

(7:3) but different spatial arrangements (AuAg alloy/C and physically mixed Au/C + Ag/C), together with single-component Au/C and Ag/C references, were evaluated under identical zero-gap conditions and all degraded within ~60–95 h (Fig. S17), indicating that the enhanced durability is associated with the catalyst-layer organization rather than with composition or with commercial Ag alone.

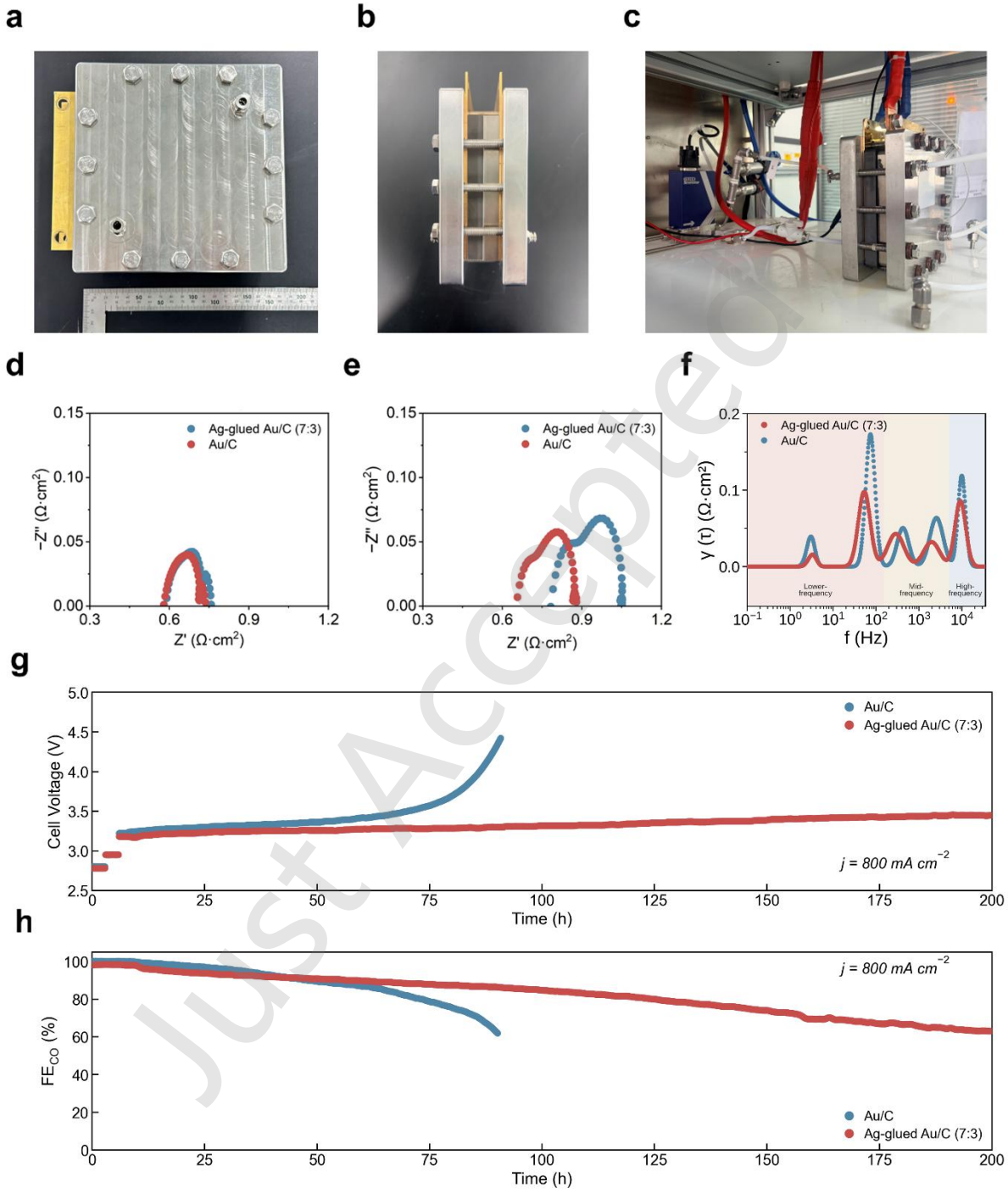


Figure 5. Engineering-scale validation of Ag-glued Au/C in a zero-gap electrolyzer. (a) Front-view photograph of the assembled zero-gap electrolyzer. (b) Side-view photograph of the assembled zero-gap electrolyzer. (c) Photograph of the electrolyzer installed on the CO_2 electrolysis test bench. (d) Nyquist plots of Au/C and Ag-glued Au/C measured 1 h after startup. (e) Nyquist plots of Au/C and Ag-glued Au/C measured after 60 h of operation. (f) DRT profiles of Au/C and Ag-glued Au/C recorded after 60 h of operation, before failure of the Au/C electrode. (g) Cell-voltage profiles of Au/C and Ag-glued Au/C during long-term operation at 800 mA cm^{-2}. (h) FE_{CO} profiles of Au/C and Ag-glued Au/C during long-term operation at 800 mA cm^{-2}.

To place this large-area zero-gap performance in context, we compiled representative state-of-the-art CO_2-to-CO electrolyzers in Table S5, comparing catalyst/cathode, electrolyzer configuration, active area, high-rate performance, stability condition, and CO selectivity. Although several reported systems have achieved excellent CO selectivity, long operation time, or high peak current density, these metrics are often demonstrated under different active areas or stability-current conditions. Ag-

Just Accepted

glued Au/C (7:3) provides a competitive combination of a 100 cm^2 active area, sustained operation at 800 mA cm^{-2}, and 200 h durability in a zero-gap MEA electrolyzer, with a voltage decay rate of 1.3 mV h^{-1} and an FE_{CO} decay rate of 0.122% h^{-1}. This comparison highlights the practical relevance of the Ag-glued catalyst-layer architecture for durable high-current-density CO_2-to-CO electrolysis.

The role of the embedded phase was further examined by replacing the large Ag particles with large Au particles (Au-glued Au/C (7:3)) or with insulating SiO_2 spheres (SiO_2-glued Au/C (7:3)), while keeping the nano-Au/C matrix, the ionomer-to-carbon ratio and the electrode fabrication protocol unchanged (Text S1 and Figs. S20–S21). All three electrodes were operated in zero-gap configuration at 800 mA cm^{-2} under identical conditions and initially delivered high CO selectivity, but their durability differed substantially (Fig. S22). SiO_2-glued Au/C underwent an abrupt voltage rise with a concurrent steep FE_{CO} decay within ca. 20 h, a response characteristic of catalyst-layer flooding. Au-glued Au/C degraded progressively and reached the 4.0 V cutoff after ca. 68 h. Ag-glued Au/C operated for 200 h with a voltage rise of ca. 0.25 V, reaching a comparable FE_{CO} level only after roughly three times longer operation.

Since all three electrodes share a large-particle/nano-matrix architecture, the size contrast alone does not account for these differences. The observed sequence instead tracks the nature of the embedded phase: the insulating, catalytically inactive SiO_2 gives the shortest lifetime, the conductive and CO_2-active but less stable large Au gives an intermediate lifetime, and Ag gives the most durable operation. Embedding a secondary phase into a nano-Au/C layer therefore appears beneficial only when that phase is electronically integrated with the matrix and remains structurally stable under sustained high-current operation. This interpretation is in line with the behaviour of Ag-based gas diffusion electrodes in practical CO_2 electrolysis: commercially available Ag-based electrodes adapted from industrial oxygen-depolarized cathodes have sustained continuous gas-fed operation for more than 1200 h at 300 mA cm^{-2} [36], indicating that Ag surfaces are compatible with maintaining a gas-accessible three-phase environment over prolonged high-rate operation. The large Ag particles embedded here may therefore help preserve gas-accessible pathways within the catalyst layer, whereas neither the insulating SiO_2 nor the large Au particles appear to provide a comparable effect.

To probe the local transport environment under operation, we performed flow-rate-modulated operando EIS with DRT analysis on Ag-glued Au/C, Au-glued Au/C and Au/C, stepping the cathode CO_2 flow rate from 1000 to 3000 sccm and back to 1000 sccm (Text S9 and Fig. S23). At the initial 1000 sccm step, Au/C shows markedly larger relaxation features than Ag-glued Au/C, most notably near 10^2 Hz, where its $\gamma(\tau)$ is roughly twice that of Ag-glued Au/C, and its flow-sensitive features respond more strongly to increasing flow rate. This indicates that local CO_2 availability in Au/C is limited by gas supply, whereas the weaker response of Ag-glued Au/C suggests that its local CO_2 supply is not limited at the nominal flow rate. The two glued electrodes display comparable magnitudes and flow-rate responses during the upward flow steps, consistent with the large-particle/nano-matrix architecture providing similar gas-transport pathways at this stage. The key difference emerges on returning to 1000 sccm: the flow-sensitive features of Ag-glued Au/C, including the low-frequency feature near 10^{-2} Hz, return close to their initial magnitudes, whereas those of Au-glued Au/C and Au/C rise above their initial values. This indicates that the local transport environment of Au-glued Au/C and Au/C does not recover after the flow perturbation, consistent with liquid accumulation in the catalyst layer that impairs CO_2 access. The reversible response of Ag-glued Au/C suggests that its catalyst layer retains gas-accessible pathways under the same perturbation, in line with reports that Ag-based gas diffusion electrodes sustain prolonged gas-fed operation [36] and with the weaker dependence of its FE_{CO} and cell voltage on the CO_2 feed rate (Fig. S19).

3.5 Mechanistic interpretation and scope

We present the following as an interpretation constrained by the available evidence rather than as a directly resolved mechanism. The most operation-relevant evidence in this study is the in-operation impedance behavior. The Nyquist responses of Au/C and Ag-glued Au/C (7:3) are nearly identical at 1 h (Fig. 5d) but diverge after 60 h of continuous operation (Fig. 5e); the DRT analysis localizes the larger growth for Au/C to a low-frequency (1–10 Hz) feature commonly associated with mass-transport-related processes (Fig. 5f); and the long-term voltage and FE_{CO} decay curves follow this same divergence (Fig. 5g,h). Read together with the fixed-composition flow-cell contrast (Fig. 4 and Table S4) and the comparable composition and limited surface-state difference of the 7:3 catalysts (Fig. 2 and Tables S1–S3), these data indicate that the durability advantage of Ag-glued Au/C (7:3) is expressed primarily as slower impedance growth and a slower evolution of the transport environment under sustained high-current operation, rather than as a composition- or surface-state-level effect. We treat this impedance- and transport-environment reading as the evidence-supported core of the interpretation. The further structural reading—that this slower impedance growth reflects better preservation of transport pathways within the catalyst layer—is consistent with these observations and with the control-particle and flow-rate-modulated DRT results (Figs. S22–S23), although the relative partitioning of Au and Ag contributions is not quantified here.

Structurally, Ag-glued Au/C combines Ag particles in the tens-to-low-hundreds-of-nanometers range with a nano-Au/C matrix built from ca. 3–5 nm Au particles on carbon black. This pronounced size contrast may produce a catalyst layer that differs from both the alloy reference and the fully nanoscale Au/C + Ag/C reference in how porosity and local pathways are organized across length scales. Under sustained high-current operation in a zero-gap configuration, the catalyst layer must simultaneously sustain CO_2 access, ionic conduction, and liquid-water removal [30-32]. In this context, embedding large Ag domains within the finer Au/C matrix may help the catalyst layer retain transport pathways during operation [15, 18]. This interpretation is broadly consistent with the slower impedance growth, weaker low-frequency DRT response, and improved voltage stability observed for Ag-glued Au/C (7:3) at 10 cm × 10 cm. The Ag-glued Au/C layer is markedly less sensitive to the CO_2 feed rate than the Au/C layer, retaining higher FE_{CO} and lower cell voltage even at reduced feed rates (Fig. S19), and its flow-sensitive DRT features are smaller and largely reversible (Figs. S23). This indicates a more favorable local gas-transport and water-removal environment within the Ag-glued Au/C layer,

Just Accepted

which sustains sufficient CO_2 supply to the active sites without relying on excess external gas flow.

A second consideration is that the embedded Ag phase is not only structural but also catalytically relevant, because Ag itself is active for CO_2-to-CO conversion. In Ag-glued Au/C, the catalyst layer therefore contains two CO-selective populations: nano-Au sites distributed throughout the Au/C matrix and larger Ag domains embedded within that matrix. Because these Ag domains are much larger than the nano-Au particles, they may remain locally functional under conditions that progressively compromise part of the finer Au/C network. In this regard, the embedded Ag phase may help preserve CO-selective behavior during prolonged operation, even as some nano-Au sites become less accessible over time. We regard this catalytic-redundancy effect as a secondary, supporting factor rather than the primary origin of the durability gain, with its quantitative role delimited as noted above.

We further note that the benefit is not metal-agnostic: large particles of non-coinage metals would introduce competing pathways—Cu toward C_{2+}/CH_4, and Sn, Bi, In, or Pb toward formate—lowering CO selectivity, whereas large Au, although CO-selective, gave a markedly shorter zero-gap lifetime than Ag in the present tests (Fig. S22) and would also be cost-prohibitive at industrial current density [33–35].

In summary, the evidence-supported core of this interpretation is that the durability advantage of Ag-glued Au/C (7:3) is expressed primarily as slower impedance growth and a slower evolution of the transport environment under sustained 800 mA cm^{-2} operation, as captured by the in-operation Nyquist, DRT, and long-term decay data (Fig. 5d–h). The accompanying structural reading—that this reflects better preservation of transport pathways within the catalyst layer—is consistent with these observations and with the control-particle and operando DRT results, whereas the detailed partitioning of Au and Ag contributions is not quantified here. Within this scope, the present results support the view that embedding large Ag nanoparticles into a nano-Au/C catalyst layer is associated with more stable CO_2-to-CO electrolysis at industrial current density.

4 Conclusions

Taken together, the present work shows that an Ag-glued Au/C catalyst layer, in which large Ag nanoparticles are physically embedded within a nano-Au/C matrix, is associated with more durable CO_2-to-CO electrolysis at industrial current density. In a zero-gap electrolyzer operated galvanostatically at 800 mA cm^{-2}, Ag-glued Au/C degraded substantially more slowly in both cell voltage and CO selectivity over 200 h, with a voltage decay rate of 1.3 mV h^{-1} and an FE_{CO} decay rate of 0.12% h^{-1}, although FE_{CO} still declined from 96% to 63% over this period. Fixed-composition comparisons further indicate that composition alone does not account for the observed differences. Control experiments replacing the embedded Ag with large Au or insulating SiO_2 particles further indicate that the durability gain is not a generic consequence of a bimodal catalyst-layer architecture. Consistent with the in-operation impedance and transport-environment evidence (Fig. 5d–h), these results point to catalyst-layer organization, beyond composition, as a practical design lever for durable CO_2-to-CO electrolysis at industrial current density, while the site-partitioning aspect of the mechanism is not quantified here. This may offer a useful reference point for other high-current-density CO_2 electrolysis systems in which durability, rather than initial selectivity, is the limiting constraint.

Electronic Supplementary Material: Experimental details; supplementary TEM, SEM, EDS, TGA, and XPS characterization; flow cell and MEA setup schematics; additional electrochemical data (Figures S1–S23, Tables S1–S5, and Texts S1–S9) are available in the online version of this article at https://doi.org/10.26599/NR.2026.94909274.

Data availability

All data needed to support the conclusions in the paper are presented in the manuscript and/or the Electronic Supplementary Material. Additional data related to this paper may be requested from the corresponding author upon request.

Acknowledgements

This work was financially supported by Shanghai Electric Group Co., Ltd. Central Academe; Feynman Dynamics Co., Ltd.; and Zhongke Yunyan (Shandong) Information Technology Co., Ltd.

Declaration of competing interest

All the contributing author(s) report(s) no conflict of interests in this work.

Author contribution statement

S.W. designed and performed the experiments, analyzed the data, prepared the figures, and wrote the manuscript. X.W., W.Y., Q.R., and A.A. assisted with experiments, characterization, data analysis, and manuscript revision. S.H. supervised the project, guided data interpretation, and revised the manuscript. All authors approved the final manuscript.

Informed consent

Not applicable

Ethics statement

Not applicable

Use of AI statement

None

References

[1] Ross, M. B.; de Luna, P.; Li, Y.; Dinh, C.-T.; Kim, D.; Yang, P.; Sargent, E. H. Designing materials for electrochemical carbon dioxide recycling. Nat. Catal. 2019, 2, 648–658.

[2] Shin, H.; Hansen, K. U.; Jiao, F. Techno-economic assessment of low-temperature carbon dioxide electrolysis. Nat. Sustain. 2021, 4, 911–919.

[3] Xia, R.; Overa, S.; Jiao, F. Emerging electrochemical processes to decarbonize the chemical industry. JACS Au 2022, 2, 1054–1070.

[4] Ge, L.; Rabiee, H.; Li, M. R.; Subramanian, S.; Zheng, Y.; Lee, J. H.; Burdyny, T.; Wang, H. Electrochemical CO_2 reduction in membrane-electrode assemblies. Chem 2022, 8, 663–692.

[5] Lees, E. W.; Mowbray, B. A. W.; Parlane, F. G. L.; Berlinguette, C. P. Gas diffusion electrodes and membranes for CO_2 reduction electrolyzers. Nat. Rev. Mater. 2022, 7, 55–64.

[6] Rabinowitz, J. A.; Kanan, M. W. The future of low-temperature carbon dioxide electrolysis depends on solving one basic problem. Nat. Commun. 2020, 11, 5231.

[7] Tan, Y. C.; Quek, W. K.; Kim, B.; Sugiarto, S.; Oh, J.; Kai, D.

Just Accepted

Pitfalls and protocols: Evaluating catalysts for CO_2 reduction in electrolyzers based on gas diffusion electrodes. ACS Energy Lett. 2022, 7, 2012–2023.

[8] Higgins, D.; Hahn, C.; Xiang, C.; Jaramillo, T. F.; Weber, A. Z. Gas-diffusion electrodes for carbon dioxide reduction: A new paradigm. ACS Energy Lett. 2019, 4, 317–324.

[9] Deng, X.; Wang, S.; Ren, Q.; Yan, X.; Zhao, W.; Cui, J.; Hu, S. High-loading Au nanoparticles on carbon by engineering surface charge and specific surface area of substrates. Prog. Nat. Sci.: Mater. Int. 2024, 34, 637–642.

[10] Zhu, W.; Michalsky, R.; Metin, O.; Lv, H.; Guo, S.; Wright, C. J.; Sun, X.; Peterson, A. A.; Sun, S. Monodisperse Au nanoparticles for selective electrocatalytic reduction of CO_2 to CO. J. Am. Chem. Soc. 2013, 135, 16833–16836.

[11] Goyal, A.; Marcandalli, G.; Mints, V. A.; Koper, M. T. M. Competition between CO_2 reduction and hydrogen evolution on a gold electrode under well-defined mass transport conditions. J. Am. Chem. Soc. 2020, 142, 4154–4161.

[12] Back, S.; Yeom, M. S.; Jung, Y. Active sites of Au and Ag nanoparticle catalysts for CO_2 electroreduction to CO. ACS Catal. 2015, 5, 5089–5096.

[13] Park, J. W.; Choi, W.; Noh, J.; Park, W.; Gu, G. H.; Park, J.; Jung, Y.; Song, H. Bimetallic gold–silver nanostructures drive low overpotentials for electrochemical carbon dioxide reduction. ACS Appl. Mater. Interfaces 2022, 14, 6604–6614.

[14] Yun, H.; Choi, W.; Shin, D.-J.; Oh, H.-S.; Hwang, Y. J. Atomic arrangement of AuAg alloy on carbon support enhances electrochemical CO_2 reduction in membrane electrode assembly. ACS Catal. 2023, 13, 9302–9312.

[15] Li, M.; Yang, W.; Wang, S.; Zhao, W.; Hu, S. Tri-phase interface regulation of ionomer-encapsulated Ag/C catalyst for industrial CO_2 electrolyzer: A DOE-based analysis. Nano Res. 2025, 18, 94907611.

[16] Li, J.; Chen, G. X.; Zhu, Y. Y.; Liang, Z.; Pei, A.; Wu, C. L.; Wang, H. X.; Lee, H. R.; Liu, K.; Chu, S.; et al. Efficient electrocatalytic CO_2 reduction on a three-phase interface. Nat. Catal. 2018, 1, 592–600.

[17] Xing, Z.; Hu, L.; Ripatti, D. S.; Hu, X.; Feng, X. Enhancing carbon dioxide gas-diffusion electrolysis by creating a hydrophobic catalyst microenvironment. Nat. Commun. 2021, 12, 136.

[18] Ko, Y. J.; Lim, C.; Jin, J.; Kim, M. G.; Lee, J. Y.; Seong, T.-Y.; Lee, K.-Y.; Min, B. K.; Choi, J.-Y.; Noh, T.; et al. Extrinsic hydrophobicity-controlled silver nanoparticles as efficient and stable catalysts for CO_2 electrolysis. Nat. Commun. 2024, 15, 3356.

[19] Du, X. W.; Zhang, P.; Zhang, G.; Gao, H.; Zhang, L. L.; Zhang, M. M.; Wang, T.; Gong, J. L. Confinement of ionomer for electrocatalytic CO_2 reduction reaction via efficient mass transfer pathways. Natl. Sci. Rev. 2024, 11, nwad149.

[20] Salvatore, D. A.; Weekes, D. M.; He, J. F.; Dettelbach, K. E.; Li, Y. C.; Mallouk, T. E.; Berlinguette, C. P. Electrolysis of gaseous CO_2 to CO in a flow cell with a bipolar membrane. ACS Energy Lett. 2018, 3, 149–154.

[21] Endrődi, B.; Kecsenovity, E.; Samu, A.; Halmágyi, T.; Rojas-Carbonell, S.; Wang, L.; Yan, Y.; Janáky, C. High carbonate ion conductance of a robust PiperION membrane allows industrial current density and conversion in a zero-gap carbon dioxide electrolyzer cell. Energy Environ. Sci. 2020, 13, 4098–4105.

[22] Petrov, K. V.; Koopman, C. I.; Subramanian, S.; Koper, M. T. M.; Burdyny, T.; Vermaas, D. A. Bipolar membranes for intrinsically stable and scalable CO_2 electrolysis. Nat. Energy 2024, 9, 932–938.

[23] De Jesus Gálvez-Vázquez, M.; Moreno-García, P.; Xu, H.; Hou, Y. H.; Hu, H. F.; Montiel, I. Z.; Rudnev, A. V.; Alinejad, S.; Grozovski, V.; Wiley, B. J.; et al. Environment matters: CO_2RR electrocatalyst performance testing in a gas-fed zero-gap electrolyzer. ACS Catal. 2020, 10, 13096–13108.

[24] Alinejad, S.; Quinson, J.; Li, Y.; Kong, Y.; Reichenberger, S.; Barcikowski, S.; Broekmann, P.; Arenz, M. Optimizing the use of a gas diffusion electrode setup for CO_2 electrolysis imitating a zero-gap MEA design. J. Catal. 2024, 429, 115209.

[25] Larrazábal, G. O.; Strøm-Hansen, P.; Heli, J. P.; Zeiter, K.; Therkildsen, K. T.; Chorkendorff, I.; Seger, B. Analysis of mass flows and membrane crossover in CO_2 reduction at high current densities in an MEA-type electrolyzer. ACS Appl. Mater. Interfaces 2019, 11, 41281–41288.

[26] Yang, K.; Li, M.; Subramanian, S.; Burdyny, T.; Vermaas, D. A.; Smith, W. A. Cation-driven increases of CO_2 utilization in a bipolar membrane electrode assembly for CO_2 electrolysis. ACS Energy Lett. 2021, 6, 4291–4298.

[27] Xu, Q.; Oener, S. Z.; Lindquist, G.; Wu, G.; Lucas, F.; Lindbergh, G.; Lagergren, C.; Johnston, C.; Vermaas, D. A. Integrated reference electrodes in anion-exchange-membrane electrolyzers: Impact of stainless-steel gas-diffusion layers and internal mechanical pressure. ACS Energy Lett. 2021, 6, 305–312.

[28] Hansen, K. U.; Cherniack, L. H.; Jiao, F. Voltage loss diagnosis in CO_2 electrolyzers using five-electrode technique. ACS Energy Lett. 2022, 7, 4504–4511.

[29] Nwabara, U. O.; de Heer, M. P.; Cofell, E. R.; Verma, S.; Negro, E.; Kenis, P. J. A. Towards accelerated durability testing protocols for CO_2 electrolysis. J. Mater. Chem. A 2020, 8, 22557–22571.

[30] Salvatore, D. A.; Berlinguette, C. P. Voltage matters when reducing CO_2 in an electrochemical flow cell. ACS Energy Lett. 2020, 5, 215–220.

[31] Zhang, Z.; Melo, L.; Jansonius, R. P.; Habibzadeh, F.; Grant, E. R.; Berlinguette, C. P. pH matters when reducing CO_2 in an electrochemical flow cell. ACS Energy Lett. 2020, 5, 3101–3107.

[32] Kim, Y.; Lees, E. W.; Berlinguette, C. P. Permeability matters when reducing CO_2 in an electrochemical flow cell. ACS Energy Lett. 2022, 7, 2382–2387.

[33] Bagger, A.; Ju, W.; Varela, A. S.; Strasser, P.; Rossmeisl, J. Electrochemical CO_2 reduction: A classification problem. ChemPhysChem 2017, 18, 3266–3273.

[34] Hori, Y. Electrochemical CO_2 reduction on metal electrodes. In Modern Aspects of Electrochemistry, Vol. 42. Vayenas, C. G.; White, R. E.; Gamboa-Aldeco, M. E., Eds.; Springer: New York, 2008; pp 89–189.

[35] Kuhl, K. P.; Hatsukade, T.; Cave, E. R.; Abram, D. N.; Kibsgaard, J.; Jaramillo, T. F. Electrocatalytic conversion of carbon dioxide to methane and methanol on transition metal surfaces. J. Am. Chem. Soc. 2014, 136, 14107–14113.

[36] Haas, T.; Krause, R.; Weber, R.; Demler, M.; Schmid, G. Technical photosynthesis involving CO_2 electrolysis and fermentation. *Nat. Catal.* 2018, *1*, 32–39.

Just Accepted

Electronic Supplementary Material

Ag-glued Au/C catalyst layer for durable CO_2-to-CO electrolysis at industrial current density

Siyang Wang, Xueqin Wu, Wenrong Yang, Qianqian Ren, Abrar Amna, and Shi Hu

Department of Chemistry, School of Science, Tianjin Key Laboratory of Molecular Optoelectronic Science, Tianjin University, Tianjin 300072, China

Address correspondence to rychushi@gmail.com

Supporting information to https://doi.org/10.26599/NR.2026.94909274

Just Accepted

Text S1. Catalyst Preparation

Synthesis of Au/C.
Au/C was prepared by colloidal synthesis of Au nanoparticles followed by carbon supporting. Briefly, $HAuCl_4 \cdot 4H_2O$ (50 mg) was dissolved in a mixed solution of n-hexane and oleylamine to form solution I. In parallel, borane tert-butylamine (11 mg) was dissolved in a mixed solution of n-hexane (0.50 mL) and oleylamine (0.50 mL) to form solution II. Solution I was purged with Ar for 10 min at 40 °C under vigorous stirring, after which solution II was rapidly injected. The mixture was then reacted at 70 °C for 1 h under Ar protection, during which the solution gradually turned purple-red, indicating the formation of Au nanoparticles.

The obtained Au nanoparticles were subsequently supported on Carbon Black. Carbon was added according to a theoretical Au loading of 50 wt%. Specifically, Carbon Black was dispersed in hexane (15 mL) by sonication for 10 min. The Au nanoparticle suspension in hexane was then added, followed by another 10 min of sonication and 12 h of stirring. After loading, the product was washed with ethanol by centrifugation 2–3 times, dried at 50 °C for 24 h, and finally ground to obtain the Au/C powder. The actual metal loading of the resulting sample was typically 41–44 wt%.

Commercial Ag nanoparticles.
Commercial Ag nanoparticles were purchased from Jiangsu XFNANO Materials Co., Ltd. as silver nanopowder (stock No. 105518; product No. XFJ14; package size: 50 g). The purchasing document did not specify additional surface coating or stabilizer information. The Ag nanoparticles were used as received without further purification or chemical pretreatment. TEM and SEM characterization showed that the Ag nanoparticles exhibited a broad particle-size distribution, predominantly in the tens-to-low-hundreds-of-nanometers range (Fig. S2). These commercial Ag nanoparticles were then physically mixed with Au/C at the target Au atomic ratio to prepare Ag-glued Au/C catalysts.

Preparation of Ag-glued Au/C catalysts.
Ag-glued Au/C catalysts were prepared by physical mixing of Au/C and commercial Ag nanoparticles. The mixing ratio was controlled according to the target Au:Ag atomic ratio. Unless otherwise noted, the total metal loading was adjusted by adding additional Carbon Black to ensure consistency across samples. The powders were ground for 20 min to obtain homogeneous mixed catalysts. The actual metal loading of the mixed samples was controlled within 40–44 wt%. The representative sample discussed in the main text was Ag-glued Au/C (7:3).

Synthesis of AuAg alloy/C.
AuAg alloy/C was synthesized by a slow-heating co-reduction method in an organic medium. Briefly, $HAuCl_4 \cdot 4H_2O$ and AgOAc were added to a mixture of oleylamine, oleic acid, benzyl ether (20.0 mL), and hexadecylamine (4.0 g). The precursor mixture was stirred at 30℃until fully dissolved, then stirred for an additional 15 min under oxygen- and moisture-free conditions. The reaction mixture was then slowly heated to 150 °C and maintained at this temperature for 5 h. After natural cooling to room temperature, the alloy nanoparticles were collected by ethanol washing and centrifugation. The obtained alloy nanoparticles were then supported on carbon using the same procedure as that described for Au/C. In this work, the alloy composition used was Au:Ag = 7:3.

Synthesis of Ag/C.
Ag/C was prepared through in situ formation of Ag nanoparticles in an oleylamine-based medium followed by one-pot loading onto Carbon Black. In a 250 mL three-neck flask equipped with a condenser, gas inlet, temperature probe, and magnetic stir bar, oleylamine and oleic acid were added, and the mixture was stirred at room temperature. The system was purged with N_2 for 20 min under slight positive pressure. AgNO3 (1 g) was then added under N_2 protection, followed by stirring for 10 min to ensure homogenization. The mixture was heated to 180 °C at 5 °C min^{-1} and maintained at this temperature for 2 h to form Ag nanoparticles. After cooling to room temperature, n-hexane (80.0 mL) was added to reduce the viscosity of the reaction medium.
Separately, Carbon Black (600 mg) was dispersed in n-hexane (40.0 mL) by sonication for 30 min and then added to the reaction flask. The dispersion vessel was rinsed with n-hexane (10.0 mL), which was also transferred into the flask. The resulting suspension was vigorously stirred at room temperature for 60 min to allow Ag nanoparticles to deposit onto the carbon support. The slurry was then slowly poured into acetone (600.0 mL) under stirring, and the mixture was stirred for an additional 10 min to induce flocculation and remove excess organic ligands. The precipitate was collected by vacuum filtration, washed successively with acetone (300.0 mL, 3 × 100.0 mL) and isopropanol (300.0 mL, 3 × 100.0 mL), and finally dried at 50 °C under vacuum for 12 h to obtain the Ag/C powder. TEM analysis confirmed that the resulting Ag/C consisted of small Ag nanoparticles (ca. 3–5 nm) uniformly dispersed on the carbon support (Fig. S13).

Just Accepted

Address correspondence to First A. Firstauthor, email1; Third C. Thirdauthor, email2

Preparation of Au/C + Ag/C catalysts.
Au/C + Ag/C catalysts were prepared by physically mixing the corresponding Au/C and Ag/C powders according to the target Au:Ag atomic ratio. Additional Carbon Black was introduced when necessary to maintain a consistent total metal loading among samples. The mixed powders were thoroughly ground before use. In this work, the composition used for Au/C + Ag/C was Au:Ag = 7:3.

Preparation of Au-glued and SiO_2-glued Au/C control catalysts.
Au-glued Au/C (7:3) and SiO_2-glued Au/C (7:3) were prepared following the same protocol used for Ag-glued Au/C (7:3), with the commercial Ag nanoparticles replaced by commercial large Au particles or by monodisperse SiO_2 spheres, respectively. The nano-Au/C matrix, the additional carbon black, the grinding procedure, the ink formulation, the catalyst-to-ionomer mass ratio and the spray-coating protocol were kept identical to those of Ag-glued Au/C (7:3), and MEA assembly and zero-gap testing followed Text S2 and Text S4. Because the three embedded phases differ in density, their volume fractions within the catalyst layer are not identical; the comparison therefore addresses the chemical and electronic nature of the embedded phase at a fixed preparation protocol rather than a strictly volume-matched architecture.

Text S2. Electrode Fabrication
Fabrication of gas diffusion electrodes (GDEs) for flow-cell tests.
The cathodic gas diffusion electrodes for flow-cell measurements were prepared by ultrasonic spray coating. Catalyst inks were formulated in a mixed ethanol/water solvent (9:1, v/v) containing catalyst powder and Nafion solution as the ionomer binder. The ionomer/catalyst mass ratio was 20 wt%, and the total solids concentration of the ink was 10 mg mL^{-1}. The catalyst inks were treated by alternating magnetic stirring and ultrasonication for a total of 12 h to ensure uniform dispersion. The inks were then uniformly deposited onto carbon paper substrates (0.5 cm × 2 cm) using a spray-coating system, followed by in situ drying to obtain the gas diffusion electrodes. The total metal loading of all GDE cathodes was controlled at ca. 0.5 mg metal cm^{-2}.

Fabrication of electrodes for zero-gap electrolyzer tests.
Zero-gap membrane electrode assemblies (MEAs) were prepared by coating the cathode catalyst layer onto commercial half anode catalyst-coated membranes (half-CCMs) supplied by Feynman Dynamics Co., Ltd. The commercial half-CCMs contained an IrO_2 anode catalyst layer and a Nafion 117 membrane. Specifically, catalyst inks were prepared in ethanol/water with a solids concentration of 10 mg mL^{-1} using Nafion solution as the ionomer binder. The ionomer/catalyst mass ratio was 20 wt%. An electrochemically active area of 10 cm × 10 cm was defined for cathode coating. Au/C or Ag-glued Au/C (7:3) was used as the cathode catalyst, depending on the test, and the total metal loading was controlled at ca. 0.5 mg metal cm^{-2}.

Text S3. Flow-Cell CO_2 Electrolysis
Flow-cell electrochemical measurements were carried out in a three-electrode configuration with an electrochemically active area of 1 cm^2. The prepared gas diffusion electrode served as the cathode, a Pt plate was used as the anode, a Nafion 117 membrane supplied by Feynman Dynamics Co., Ltd. was used as the separator, and an Ag/AgCl electrode was employed as the reference electrode. During electrolysis, dry CO_2 was fed to the cathode side at 20 sccm without external humidification, while 0.5 M $KHCO_3$ was circulated on the anode side at 10 mL min^{-1}. All flow-cell tests were conducted at room temperature (25 ± 2 °C) under potentiostatic control.
All potentials reported in this work were converted to the reversible hydrogen electrode (RHE) scale according to:

$$E_{RHE} = E_{Ag/AgCl} + 0.197 + 0.0591 \times pH$$

Gas products were analyzed using an online gas chromatograph (GC), and CO, H_2, and unreacted CO_2 were quantified. The Faradaic efficiency (FE) of each gaseous product was calculated according to:

$$FE_i = \frac{z_i F n_i}{I} \times 100\%$$

where z_i is the number of electrons transferred for forming one molecule of product i, F is the Faraday constant, n_i is the production rate of product i, and I is the total current.
The partial current density of each product was calculated using:

Just Accepted

$$j_i = j_{total} \times \frac{FE_i}{100}$$

where j_i is the partial current density of product i, $j_{total}$is the total current density, and FE_i is the corresponding Faradaic efficiency.
Liquid products were not analyzed.

Text S4. Zero-Gap Electrolyzer Operation and Long-Term Testing
During zero-gap electrolyzer operation, dry CO_2 was supplied to the cathode side at 1200 sccm without external humidification, while 0.5 M $KHCO_3$ was fed to the anode side at 200 mL min^{-1}. The zero-gap MEA used a commercial half-CCM supplied by Feynman Dynamics Co., Ltd., containing an IrO_2 anode catalyst layer and a Nafion 117 membrane. The cathode catalyst layer was prepared using Nafion solution as the ionomer binder, with an ionomer/catalyst mass ratio of 20 wt%. Long-term electrolysis was performed at 40 °C under galvanostatic operation, with the current stepped from 30 A to 60 A (3 h each) and then held at 80 A, corresponding to a current density of 800 mA cm^{-2}. Both Au/C and Ag-glued Au/C (7:3) were evaluated in the zero-gap electrolyzer configuration, and Ag-glued Au/C (7:3) was further operated continuously for 200 h under the same conditions. Gas products were analyzed by online gas chromatography, and the product quantification and Faradaic efficiency calculations followed the methods described in Text S3. Distribution of relaxation times (DRT) analysis was performed on electrochemical impedance spectroscopy (EIS) spectra acquired over a frequency range of 0.1 Hz to 100 kHz. To verify that no additional features were present at lower frequencies for these 60 h spectra, supplementary measurements were extended to 0.01 Hz, and no additional DRT peaks were resolved below 0.1 Hz for either electrode under these conditions. Flow-rate-modulated operando DRT measurements, performed under a different operating history, are described separately in Text S9.

Text S5. Calculation of CO_2 Single-Pass Utilization and Energy Efficiency
The CO_2 single-pass utilization (SPU) was calculated using the following equation:

$$\mathrm{SPU}(\%) = \frac{j \cdot A \cdot FE_{CO}}{2F \cdot \dot{n}_{CO_2}} \times 100$$

where j is the applied current density (0.8 A cm^{-2}), A is the geometric electrode area (100 cm^2), FE_{CO} is the Faradaic efficiency toward CO, F is the Faraday constant (96485 C mol^{-1}), and n_CO_2,in is the molar flow rate of CO_2 fed to the cathode.$\dot{n}_{CO_2}$ With a CO_2 feed flow rate of 1200 sccm:

$$\dot{n}_{CO_2} = \frac{1200}{60 \times 22414} = 8.92 \times 10^{-4}\ \mathrm{mol\ s^{-1}}$$

The energy efficiency (EE) was calculated as:

$$\mathrm{EE}_{CO}(\%) = \frac{E^{\circ}_{CO}}{V_{cell}} \times FE_{CO} \times 100$$

where E° = 1.33 V is the standard thermodynamic cell voltage E°_{CO} for the overall reaction $CO_2 + H_2O \rightarrow CO + ½O_2$, and V_{cell} is the measured full-cell voltage. For the Ag-glued Au/C (7:3) zero-gap electrolyzer operated at 800 mA cm^{-2}, the SPU was 44.6% at ~10 h (FE_{CO} = 96.0%, V_{cell} = 3.196 V) and decreased to 29.3% at ~200 h (FE_{CO} = 63.0%, V_{cell} = 3.446 V). The corresponding EE_CO was 40.0% at ~10 h and 24.3% at ~200 h, reflecting the progressive decline in FE_{CO} over the course of the stability test.

Just Accepted

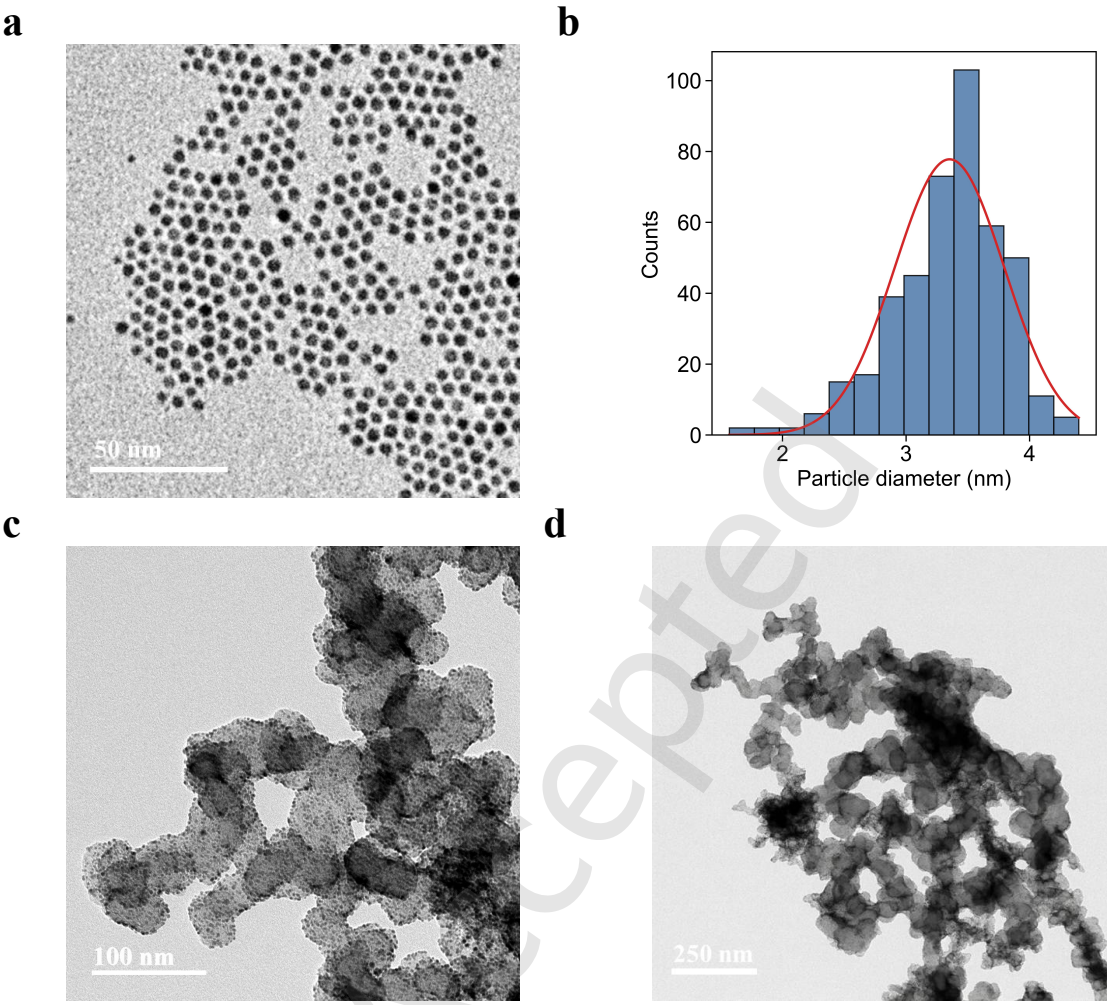


Figure S1. Additional TEM characterization of AuNPs and Au/C.
(a) Representative TEM image of AuNPs.
(b) Particle-size distribution of AuNPs derived from TEM analysis.
(c) High-magnification TEM image of Au/C, showing uniformly dispersed Au nanoparticles anchored on the carbon support.
(d) Low-magnification TEM image of Au/C.

Just Accepted

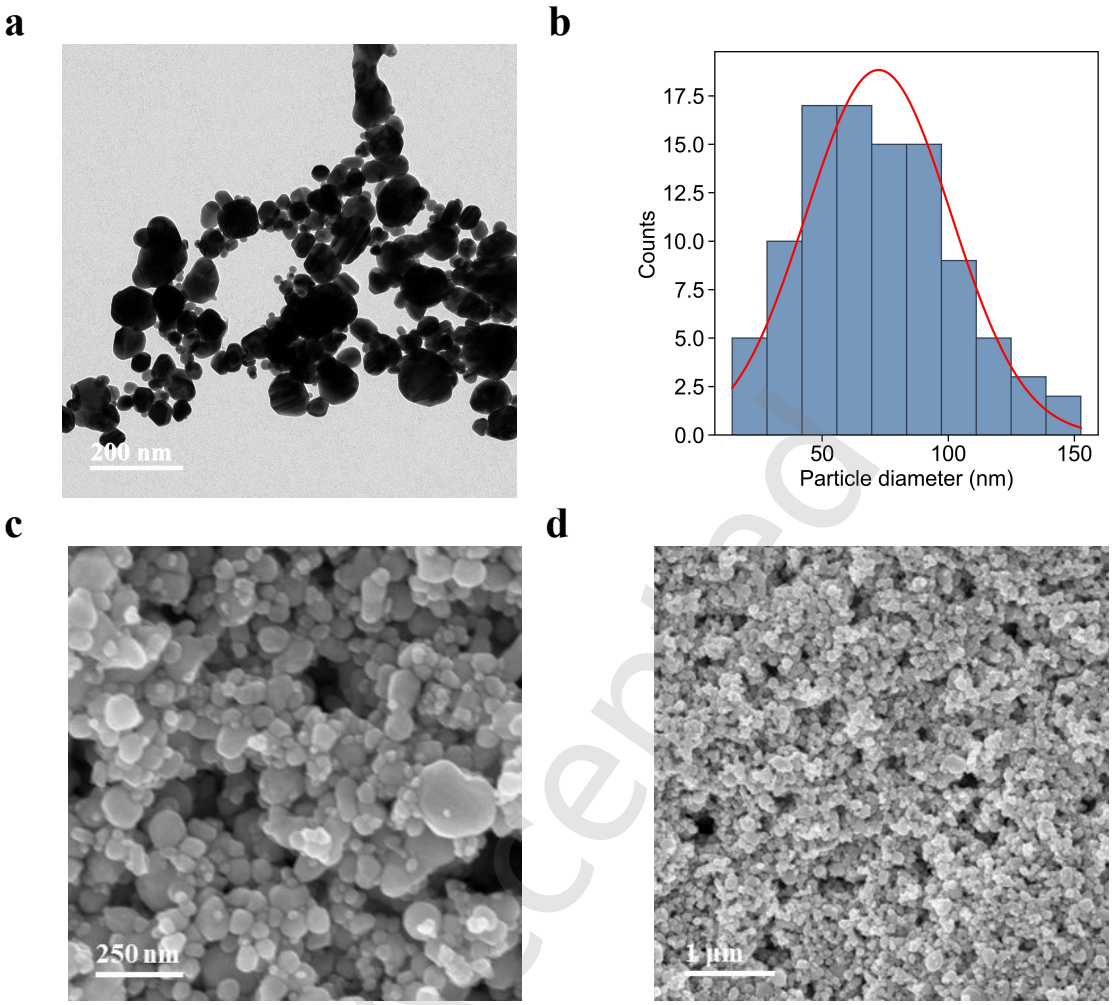


Figure S2. Additional TEM and SEM characterization of AgNPs.
(a) Representative TEM image of AgNPs.
(b) Particle-size distribution of AgNPs derived from TEM analysis.
(c) High-magnification SEM image of AgNPs.
(d) Low-magnification SEM image of AgNPs.

Just Accepted

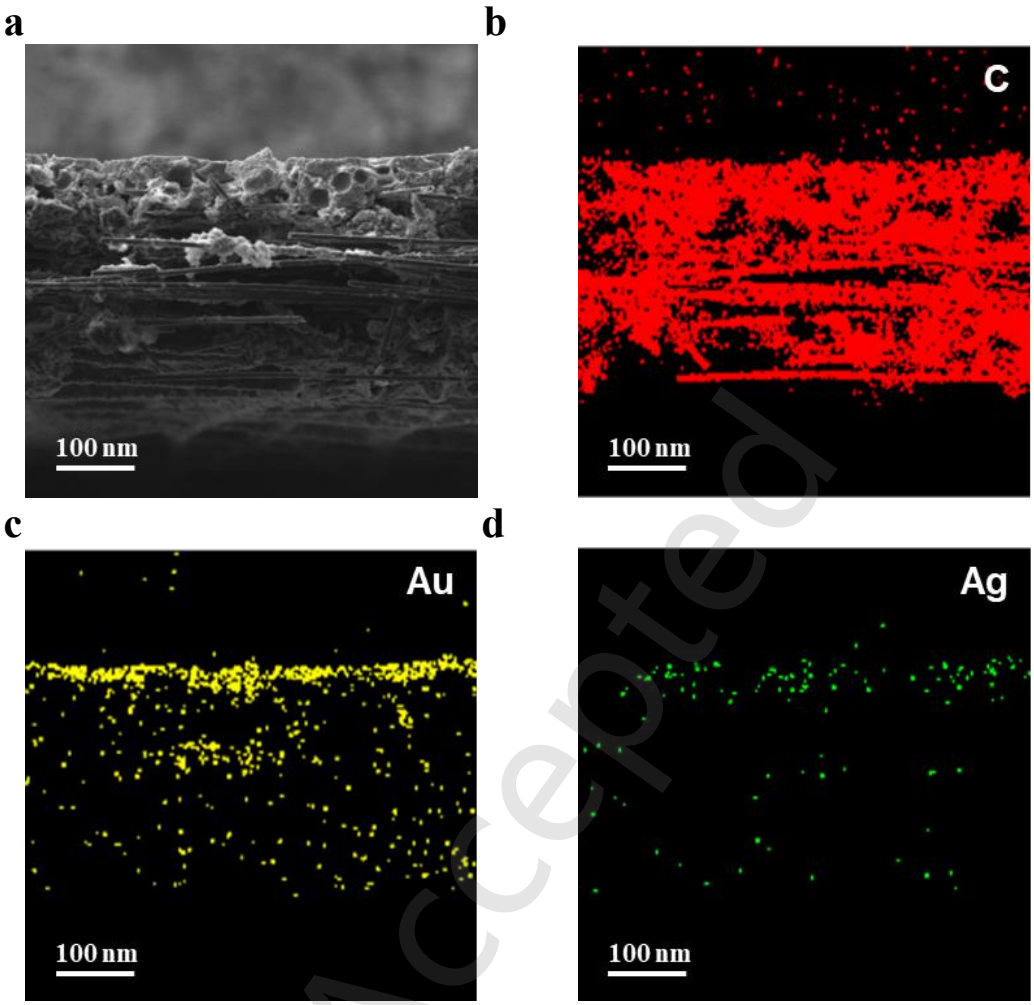


Figure S3. Cross-sectional SEM image and corresponding EDS elemental maps of the Ag-glued Au/C GDE.
(a) Cross-sectional SEM image of the Ag-glued Au/C GDE.
(b–d) Corresponding EDS elemental maps of C, Au, and Ag, respectively. The Ag signal (d) is distributed across the full thickness of the catalyst layer rather than being concentrated at the outermost surface, indicating that the large Ag nanoparticles are incorporated throughout the catalyst layer depth rather than simply piled at the surface.

Just Accepted

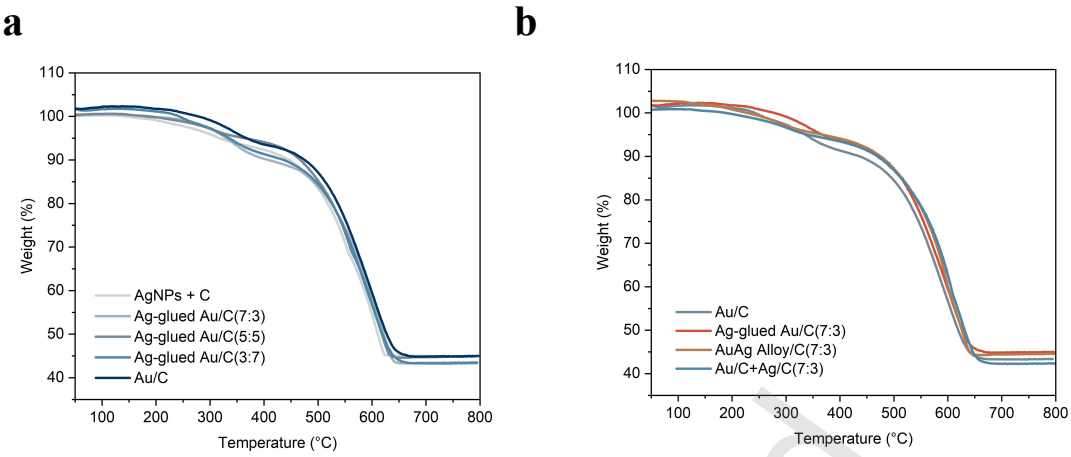


Figure S4. Representative full thermogravimetric analysis (TGA) curves of the catalyst samples. (a) TGA curves of the physically mixed Ag-glued Au/C series used for composition screening, including Au/C, Ag-glued Au/C (7:3), Ag-glued Au/C (5:5), Ag-glued Au/C (3:7), and AgNPs + C. (b) TGA curves of representative catalysts with different Au/Ag organization modes, including Au/C, Ag-glued Au/C (7:3), AuAg alloy/C (7:3), and Au/C + Ag/C (7:3). These measurements serve to verify loading comparability across samples rather than to characterize catalyst-layer structure; structural organization is addressed separately by SEM, EDS mapping, and XRD (Figs. 1 and S3).

Table S1. Residual mass ratios of the catalyst samples determined by thermogravimetric analysis (TGA) at 800 °C.

Sample	Residual mass at 800 °C			
	rep 1 (wt%)	rep 2 (wt%)	rep 3 (wt%)	mean ± SD (wt%)
Au/C	43.27	44.15	42.75	43.39 ± 0.71
Ag-glued Au/C (7:3)	45.03	44.05	44.32	44.46 ± 0.50
Ag-glued Au/C (5:5)	41.63	42.11	40.81	41.52 ± 0.66
Ag-glued Au/C (3:7)	42.84	42.52	44.44	43.27 ± 1.03
AgNPs + C	44.37	44.24	43.60	44.07 ± 0.42
AuAg Alloy/C (7:3)	44.57	42.60	42.69	43.29 ± 1.11
Au/C + Ag/C (7:3)	42.37	42.47	43.62	42.82 ± 0.70

Residual mass values were extracted from three independent TGA measurements at 800 °C and are reported as mean ± standard deviation. TGA was carried out under air from room temperature to 800 °C at a heating rate of 5 °C min^{-1}. The curves shown in Fig. S4 are representative traces. TGA here serves to verify metal-loading comparability across samples; the catalyst-layer structural organization is addressed separately by SEM, EDS mapping, and XRD (Figs. 1 and S3).

Just Accepted

Table S2. Target and measured Ag fractions of the catalyst samples determined by inductively coupled plasma optical emission spectroscopy (ICP-OES).

Sample	Target Ag fraction (%)	Measured Ag fraction (%)			
		rep 1	rep 2	rep 3	mean ± SD
Au/C	0	—	—	—	—
Ag-glued Au/C (7:3)	30	31.97	32.31	32.22	32.17 ± 0.18
Ag-glued Au/C (5:5)	50	51.12	51.03	51.35	51.17 ± 0.17
Ag-glued Au/C (3:7)	70	68.78	69.16	68.83	68.92 ± 0.21
AgNPs + C	100	—	—	—	—
AuAg Alloy/C (7:3)	30	28.13	27.68	27.58	27.79 ± 0.29
Au/C + Ag/C (7:3)	30	27.35	27.08	27.43	27.29 ± 0.18

Measured Ag fractions are reported as mean ± standard deviation from three independent ICP-OES measurements. Au/C and AgNPs + C were not included in the ICP-OES quantification of Ag fraction.

Just Accepted

Table S3. X-ray photoelectron spectroscopy (XPS) peak fitting parameters for the Au 4f and Ag 3d core-level spectra of the catalyst series.

Sample	Au $4f_{7/2}$ B.E. (eV)	Au $4f_{7/2}$ FWHM (eV)	Au $4f_{5/2}$ B.E. (eV)	Au SO splitting (eV)	Ag $3d_{5/2}$ B.E. (eV)	Ag $3d_{5/2}$ FWHM (eV)	Ag $3d_{3/2}$ B.E. (eV)	Ag SO splitting (eV)
AgNPs	—	—	—	—	368.306 ± 0.003	0.885	374.312 ± 0.004	6.006
Ag/C	—	—	—	—	368.482 ± 0.004	1.017	374.485 ± 0.005	6.003
Au/C	84.429 ± 0.006	1.127	88.091 ± 0.007	3.662	—	—	—	—
Ag-glued Au/C (7:3)	84.371 ± 0.005	1.118	88.036 ± 0.007	3.665	368.552 ± 0.011	0.936	374.571 ± 0.017	6.019
AuAg alloy/C (7:3)	84.467 ± 0.004	0.919	88.140 ± 0.006	3.673	368.441 ± 0.005	1.025	374.440 ± 0.007	5.999
Au/C + Ag/C (7:3)	84.405 ± 0.005	1.114	88.073 ± 0.007	3.668	368.601 ± 0.006	1.094	374.594 ± 0.009	5.993

XPS measurements were carried out on a Thermo Scientific spectrometer (Al Kα source, 1486.6 eV; pass energy 30 eV; step size 0.05 eV; spot size 500 μm). Binding energies were referenced to the

adventitious C 1s peak at 284.8 eV. Peak fitting was performed in Thermo Avantage software using a Smart (Shirley-type) background and a Gaussian line shape; each core-level doublet (Au $4f_{7/2}$–$4f_{5/2}$, Ag $3d_{5/2}$–$3d_{3/2}$) was fitted simultaneously. All peaks are consistent with a single metallic species (Au^0, Ag^0), and no deconvolution into oxidized sub-components ($Au3^+$, Ag^+) was performed, as no spectral evidence for such components was observed. Fit uncertainties represent one standard deviation from the least-squares fitting. FWHM denotes full width at half maximum. Entries marked "—" correspond to elements not present in the sample. The spin-orbit splittings (ca. 3.67 eV for Au 4f and ca. 6.00 eV for Ag 3d) are consistent with metallic Au^0 and Ag^0 reference values.

For the three fixed-composition (7:3) catalysts, the Au $4f_{7/2}$ binding energies of Ag-glued Au/C (7:3) and Au/C + Ag/C (7:3) differ by 0.034 eV, and the Ag $3d_{5/2}$ values differ by 0.049 eV, both within the combined fitting uncertainties. In contrast, AuAg alloy/C (7:3) shows shifts of 0.096 eV (Au $4f_{7/2}$) and 0.111 eV (Ag $3d_{5/2}$) relative to Ag-glued Au/C (7:3), consistent with electronic modification associated with alloy formation.

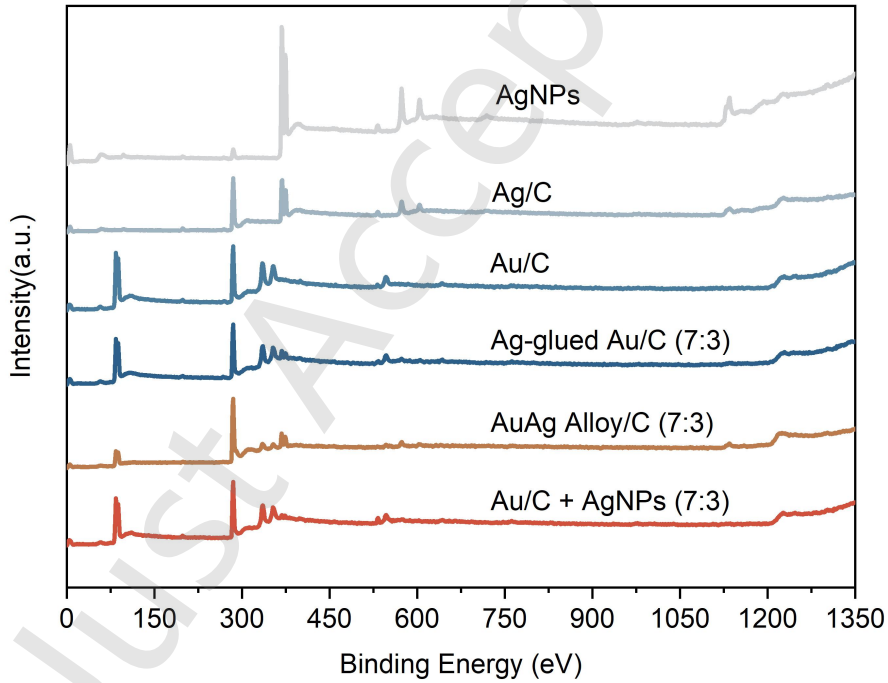


Figure S5. Stacked XPS survey spectra of Ag, Ag/C, Au/C, Au/C + Ag/C (7:3), AuAg alloy/C (7:3), and Ag-glued Au/C (7:3). The spectra are vertically offset for clarity. The major features in the survey spectra can be assigned to C 1s (~284.8 eV), O 1s (~531 eV), Au 4f (~84 and ~87.7 eV), and Ag 3d (~368 and ~374 eV), consistent with the corresponding sample compositions.

Just Accepted

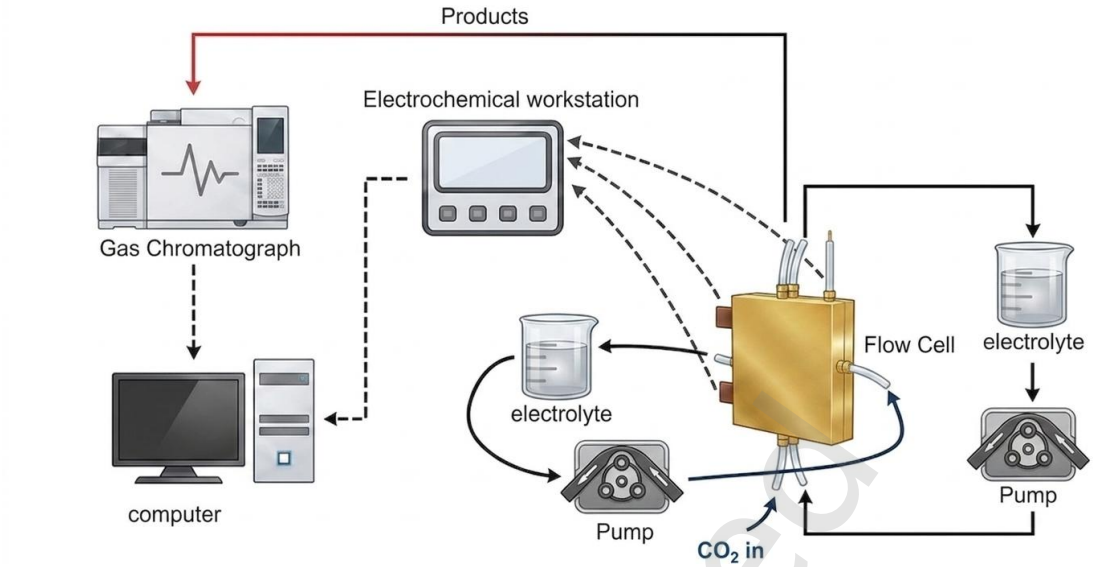


Figure S6. Schematic of the flow-cell setup used for CO_2 electrolysis. CO_2 was supplied to the cathode, and the anolyte and catholyte were circulated through the cell using peristaltic pumps. The cell was operated with an electrochemical workstation, and the outlet gas products were analyzed online by gas chromatography.

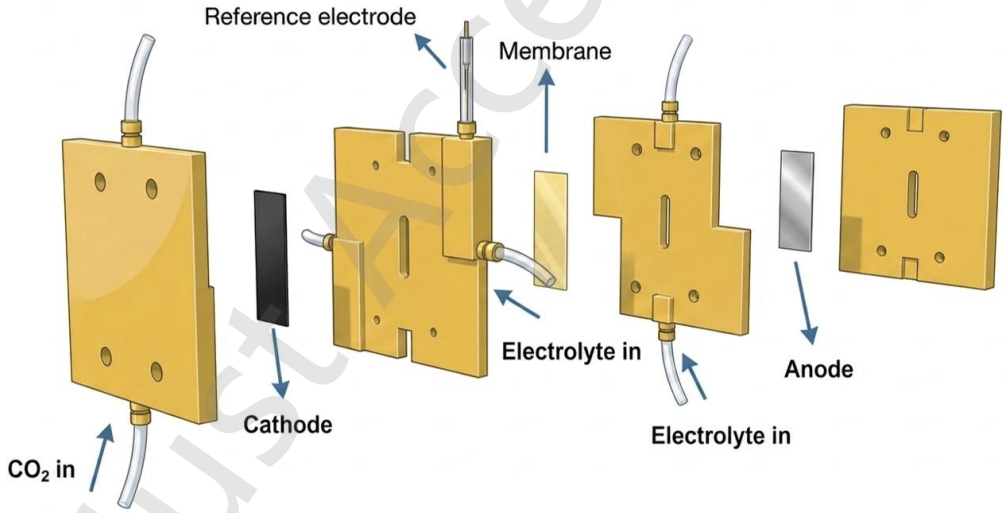


Figure S7. Exploded-view schematic of the flow cell used for CO_2 electrolysis. The cell consisted of a cathode flow-field plate, cathode electrode, membrane, anode electrode, and anode flow-field plate. CO_2 was introduced from the cathode side, while electrolyte was fed to the anode compartment. A reference electrode was incorporated for potential control during electrochemical measurements.

Just Accepted

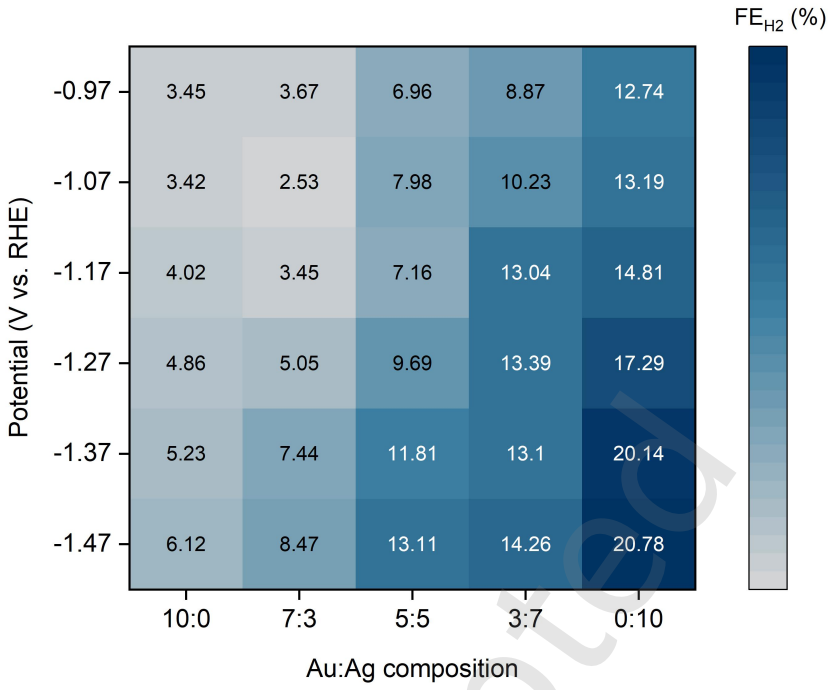


Figure S8. Composition-dependent FE_{H2} of physically mixed Ag-glued Au/C catalysts in a flow cell. Heat map of FE_{H2} for physically mixed Ag-glued Au/C catalysts with Au: Ag ratios of 10:0, 7:3, 5:5, 3:7, and 0:10 at different applied potentials.

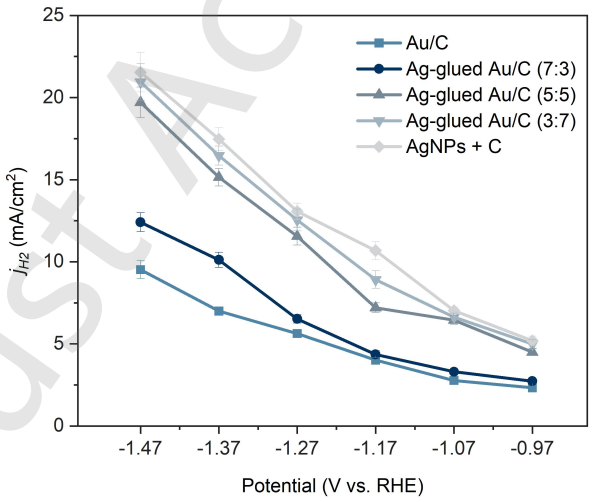


Figure S9. H_2 partial current density of physically mixed Ag-glued Au/C catalysts in a flow cell. H_2 partial current density (j_{H2}) as a function of applied potential for physically mixed Ag-glued Au/C catalysts with Au:Ag ratios of 10:0, 7:3, 5:5, 3:7, and 0:10.

Just Accepted

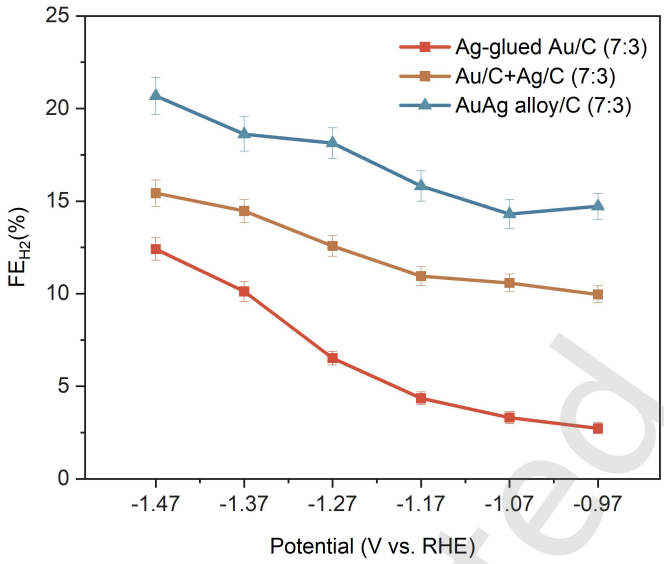


Figure S10. FE_{H2} of catalysts with different Au/Ag organization modes at a fixed Au: Ag ratio of 7:3.
FE_{H2} as a function of applied potential for Ag-glued Au/C (7:3), Au/C + Ag/C (7:3), and AuAg alloy/C (7:3).

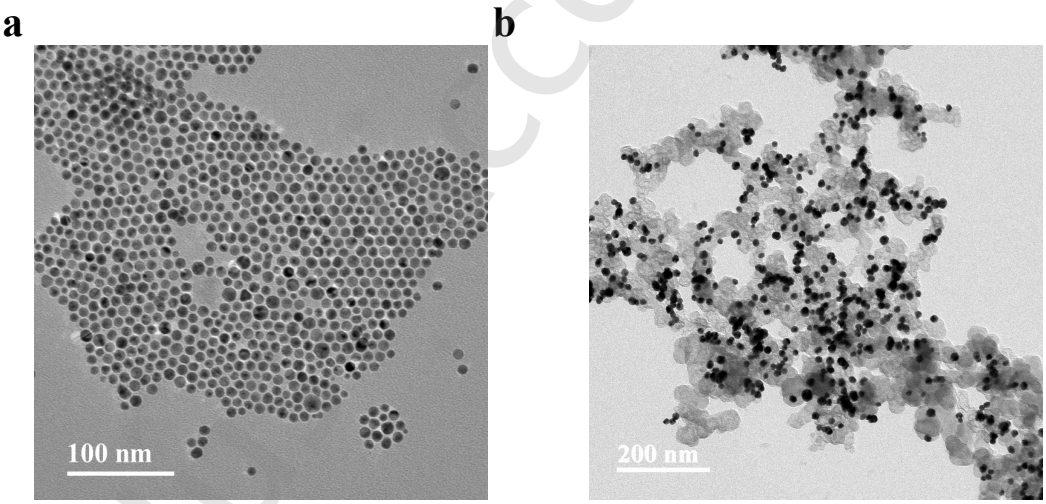


Figure S11. TEM and SEM images of AuAg alloy/C (7:3).
(a) TEM image of AuAg alloy nanoparticles.
(b) SEM image of AuAg alloy/C (7:3).

Accepted

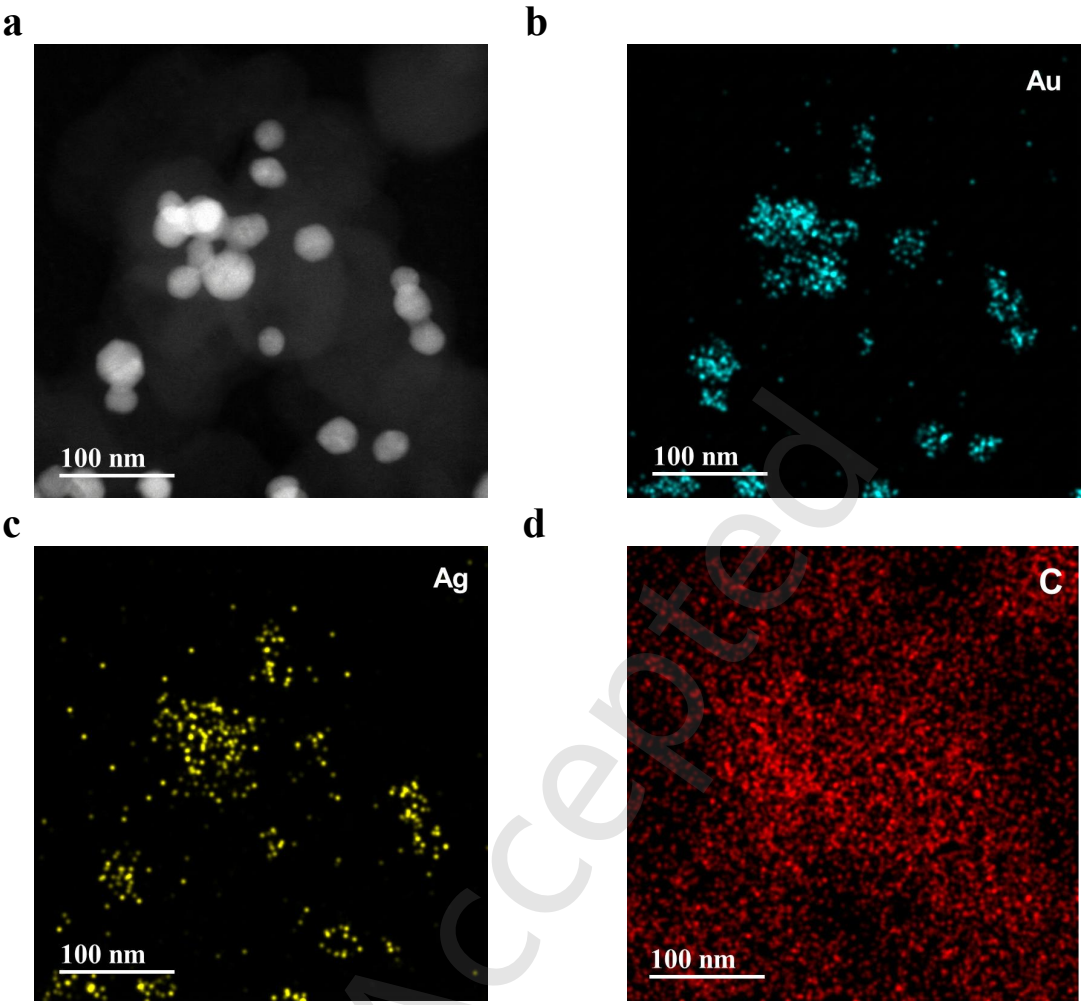


Figure S12. HAADF-STEM image and corresponding EDS elemental maps of AuAg alloy/C (7:3).
(a) HAADF-STEM image of AuAg alloy/C (7:3).
(b–d) Corresponding EDS elemental maps of Au, Ag, and C, respectively.

Just Accepted

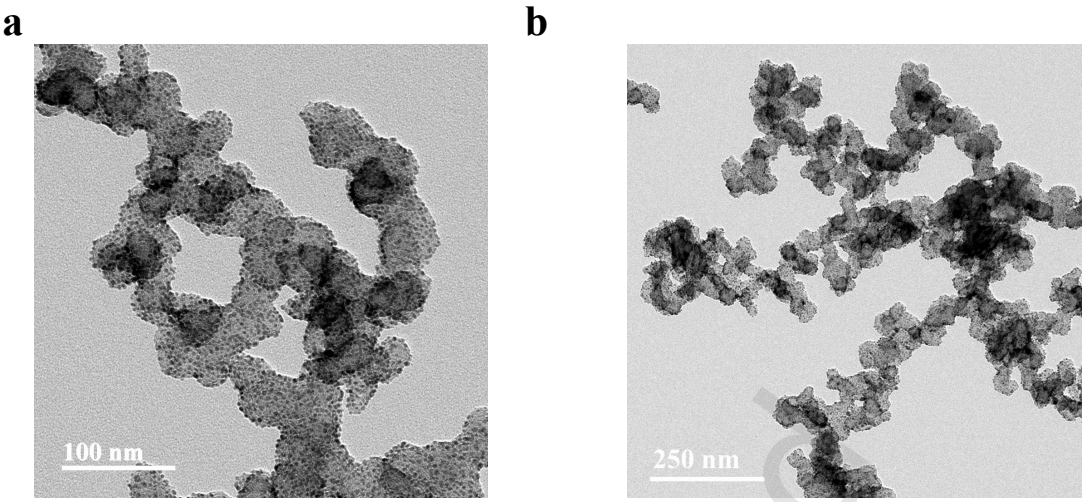


Figure S13. TEM images of Ag/C.
(a) High-magnification TEM image of Ag/C.
(b) Low-magnification TEM image of Ag/C.

Just Accepted

Text S6. Metal-mass activity and active-site utilization.
All electrodes in this study were fabricated at an identical total metal loading of 0.5 mg cm^{-2}. This fixed-loading design allows the partial CO current density (j_{CO}) measured under identical conditions to be normalized directly to the total metal mass, giving a metal-mass activity (mA mg^{-1}_metal) that reflects the device-relevant CO production rate per unit precious-metal input. j_{CO} was obtained as $j_{CO} = j_{total} \times FE_{CO}$ at −1.37 V vs. RHE (without iR correction), and the metal-mass activity was calculated as j_{CO} / 0.5 mg cm^{-2}. The results are summarized in Table S4.
For samples sharing the same nominal 7:3 composition, the Ag-glued Au/C electrode shows a higher metal-mass activity (278.1 mA mg^{-1}) than both the physically mixed Au/C + Ag/C electrode (193.9 mA mg^{-1}) and the AuAg alloy/C electrode (139.5 mA mg^{-1}). Because composition and total metal loading are held constant across these three samples, the differences cannot be ascribed to the amount or the elemental composition of the metal, and instead suggest that the catalyst-layer organization governs how effectively the available active sites are utilized under reaction conditions. A consistent trend is observed across the Ag-glued Au/C composition series, in which the 7:3 ratio gives the highest metal-mass activity among the tested compositions.
We note that this fixed-loading metal-mass activity comparison is intentionally chosen in place of an ECSA-normalized (intrinsic) activity. Electrochemically active surface area (ECSA) normalization isolates the intrinsic per-site activity by dividing out differences in accessible surface area and site number; however, this would also normalize away the local transport and organization effects that are the central subject of this work, and it is less representative of fixed-loading device operation at industrial current density. A complementary electrochemically active surface area (ECSA)-resolved and operando analysis that separately quantifies intrinsic site activity and effective utilization is identified as a direction for future work.

Table S4. Partial CO current density (j_{CO}) and metal-mass activity of the electrodes at −1.37 V vs.

RHE in the flow cell.
All electrodes have an identical total metal loading of 0.5 mg cm^{-2}. Metal-mass activity = j_{CO} / 0.5 mg cm^{-2}. Potentials are not iR-corrected. The upper block lists the Ag-glued Au/C composition series together with the Au/C and AgNPs + C end members; the lower block lists the two same-composition (nominal 7:3) reference electrodes used for the organization comparison.

Electrode	j_{CO} (mA cm^{-2})	Metal-mass activity (mA mg^{-1}_metal)
Ag-glued Au/C (7:3)	139.1	278.1
Au/C + Ag/C (7:3)	97.0	193.9
AuAg alloy/C (7:3)	69.7	139.5
Au/C	125.4	250.8
Ag-glued Au/C (5:5)	123.1	246.2
Ag-glued Au/C (3:7)	97.6	195.3
AgNPs + C	69.0	138.0

Text S7. Particle-size considerations for the AuAg alloy/C comparison.
The Ag-glued Au/C electrode and the AuAg alloy/C reference were obtained through different routes, and a direct size match between the two systems is difficult to achieve. The Au nanoparticles in Au/C are small and well dispersed (ca. 3–5 nm; Fig. S1), whereas the alloyed AuAg nanoparticles are larger (ca. 10–13 nm; Fig. S11), and the commercial Ag particles used as the "glue" are larger still and broadly distributed (tens to low hundreds of nanometers; Fig. S2). Synthesizing fully alloyed, carbon-supported AuAg nanoparticles at sizes comparable to the Au/C building blocks is challenging, mainly because the large difference in the reduction potentials of the Au and Ag precursors makes homogeneous co-reduction difficult; the conditions required to achieve compositional homogeneity (slow-heating co-reduction at elevated temperature) tend to yield larger and less uniform particles. For this reason, the AuAg alloy/C is used here as a representative of the intermixed (alloyed) AuAg configuration rather than as a size-matched control. While a contribution of particle-size differences to the observed performance and durability differences cannot be fully ruled out, the markedly different behavior across the alloyed and physically mixed references is consistent with a dominant role of catalyst-layer organization.

Just Accepted

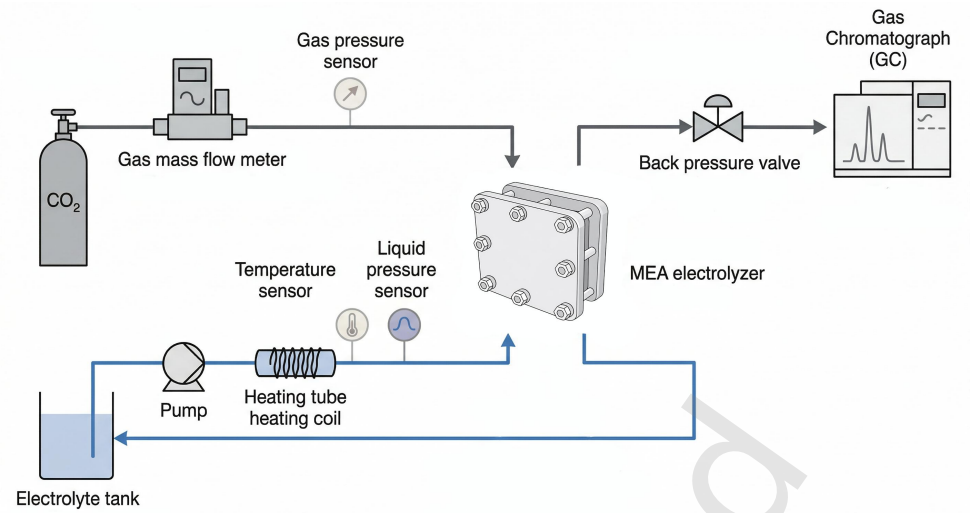


Figure S14. Schematic illustration of the electrochemical test system used for large-area (10 cm × 10 cm) MEA CO_2 electrolysis. CO_2 was supplied to the cathode side through a gas mass flow meter, and the outlet gas was passed through a back-pressure valve to an online gas chromatograph (GC) for product analysis. On the anode side, the electrolyte was circulated from the tank by a pump and preheated through a heating tube/heating coil before entering the zero-gap electrolyzer. Gas pressure, liquid pressure, and temperature sensors were integrated into the system for real-time monitoring during operation.

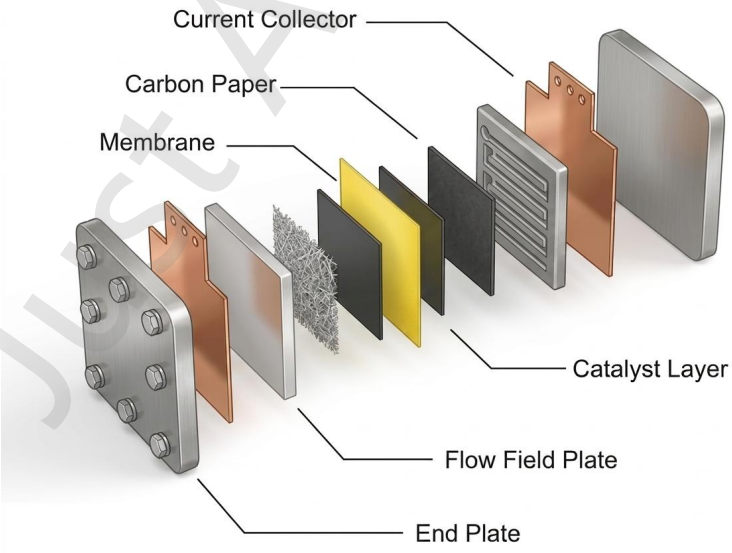


Figure S15. Exploded-view schematic of the 10 cm × 10 cm zero-gap electrolyzer used for engineering-scale CO_2 electrolysis. The assembly includes the end plates/current collectors, sealing components, flow-field plates, gas diffusion electrodes, membrane, and associated structural layers.

Just Accepted

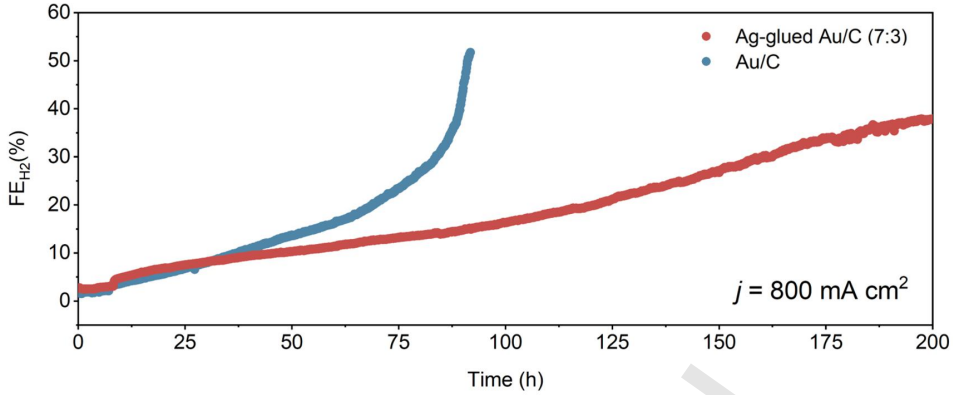


Figure S16. FE_{H2} profiles of the Au/C and Ag-glued Au/C electrodes during long-term CO_2 electrolysis. The Ag-glued Au/C electrode maintained a lower H_2 Faradaic efficiency over a substantially longer operating period, whereas the Au/C electrode showed a more rapid increase in FE_{H2} prior to failure. These results are consistent with the improved retention of CO selectivity for the Ag-glued Au/C catalyst layer under prolonged operation

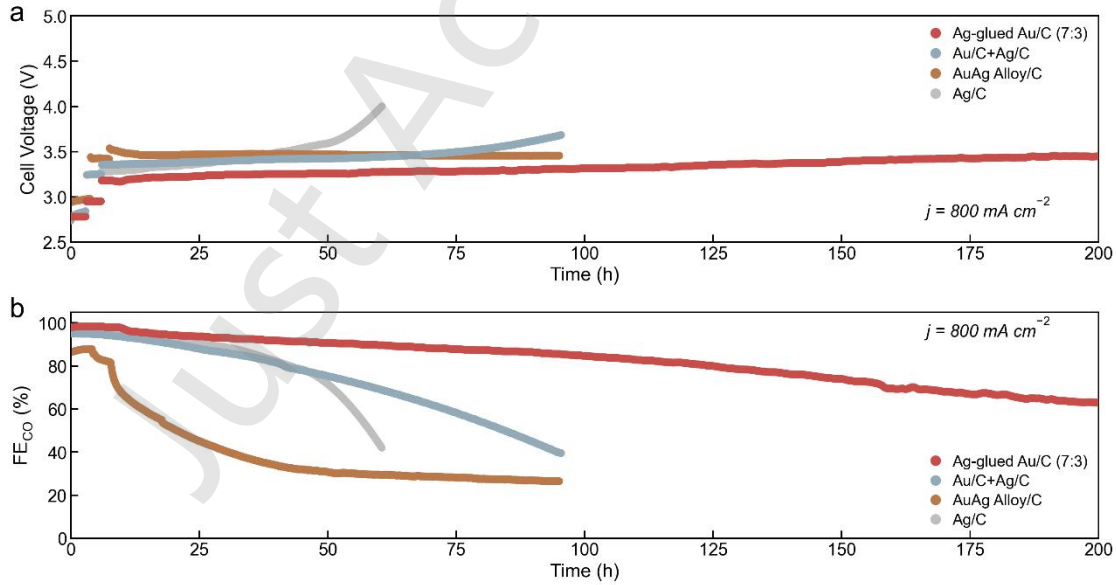


Figure S17. Long-term stability of catalyst layers with the same nominal Au:Ag composition (7:3) but different spatial organization, measured under identical zero-gap conditions at j = 800 mA cm^{-2}. (a, b) Cell voltage and FE_{CO} for Au/C, physically mixed Au/C + Ag/C, and Ag-glued Au/C. (c, d) Cell voltage and FE_{CO} for AuAg alloy/C and single-component Ag/C. All electrodes were tested with the same catalyst loading, membrane, electrolyte, and operating conditions.

Just Accepted

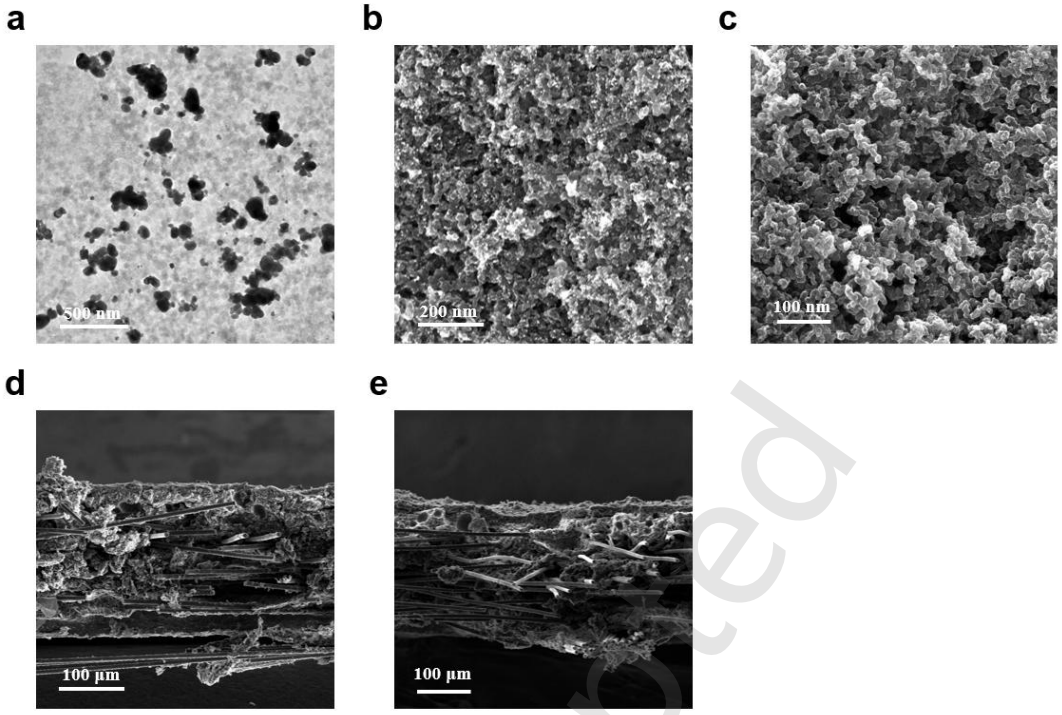


Figure S18. (a) TEM image of AgNPs + C. (b) Top-view SEM of the AuAg alloy/C (7:3) catalyst layer. (c) Top-view SEM of the Au/C + Ag/C (7:3) catalyst layer. (d, e) Cross-sectional SEM of the (d) AuAg alloy/C (7:3) and (e) Au/C + Ag/C (7:3) gas diffusion electrodes. Cross-sections were obtained by fracturing the electrodes; the dense catalyst layer sits on top of the carbon-fiber gas diffusion layer. Both electrodes were spray-coated at the same total metal loading (ca. 0.5 mg cm^{-2}) and the same catalyst-to-ionomer mass ratio of 5:1 (ionomer at 20 wt% of the catalyst). The corresponding surface and cross-sectional morphology of Ag-glued Au/C (7:3) are shown in Fig. 1d and Fig. S3, respectively.

Text S8. Catalyst-layer physical parameters of the GDEs.

To assess whether the electrochemical contrast among Ag-glued Au/C (7:3), AuAg alloy/C (7:3), and Au/C + Ag/C (7:3) could arise from bulk catalyst-layer differences rather than from the Au/Ag organization, we compared the surface morphology, cross-sectional thickness, and ionomer-to-carbon ratio of these same-composition electrodes. All were spray-coated at the same total metal loading (ca. 0.5 mg cm^{-2}) and the same catalyst-to-ionomer mass ratio of 5:1 (ionomer at 20 wt% of the catalyst). Because the TGA-derived metal contents fall within a narrow range (44.5, 43.3, and 42.8 wt% for Ag-glued Au/C, AuAg alloy/C, and Au/C + Ag/C, respectively; Table S1), the corresponding carbon contents (55.5–57.2 wt%) and ionomer-to-carbon mass ratios (0.36, 0.35, and 0.35) are nearly identical. Surface SEM (Fig. 1d and Fig. S18b, c) shows comparable porous morphologies, and cross-sectional SEM (Fig. S3 and Fig. S18d, e) shows comparably thin catalyst layers of similar thickness (on the order of tens of micrometers) on the gas diffusion layer. These results indicate that the bulk catalyst-layer parameters are comparable, so the durability divergence is not readily attributed to differences in catalyst-layer thickness, ionomer-to-carbon ratio, or surface morphology alone.

Just Accepted

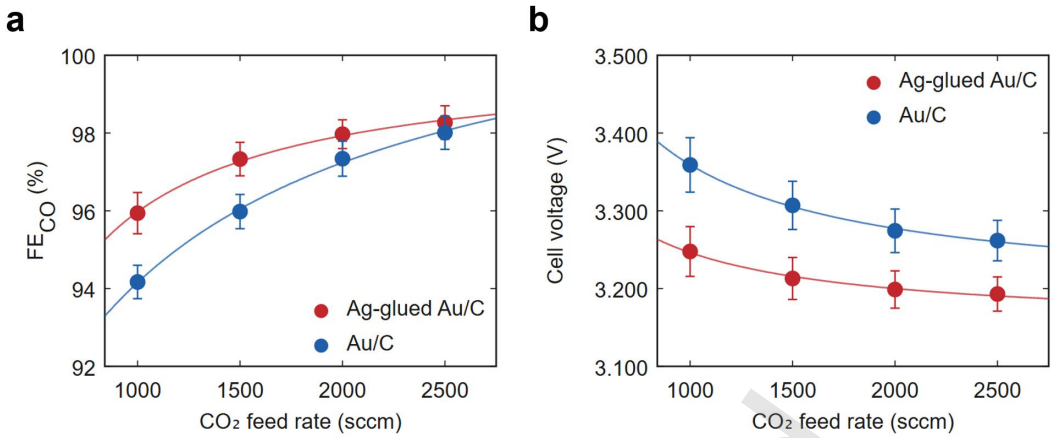


Figure S19. Effect of CO_2 feed rate on the performance of Ag-glued Au/C and Au/C catalyst layers in the 10 cm × 10 cm zero-gap electrolyzer at 800 mA cm^{-2}. (a) FE_{CO} and (b) cell voltage as a function of CO_2 feed rate (1000–2500 sccm) for Ag-glued Au/C and Au/C.

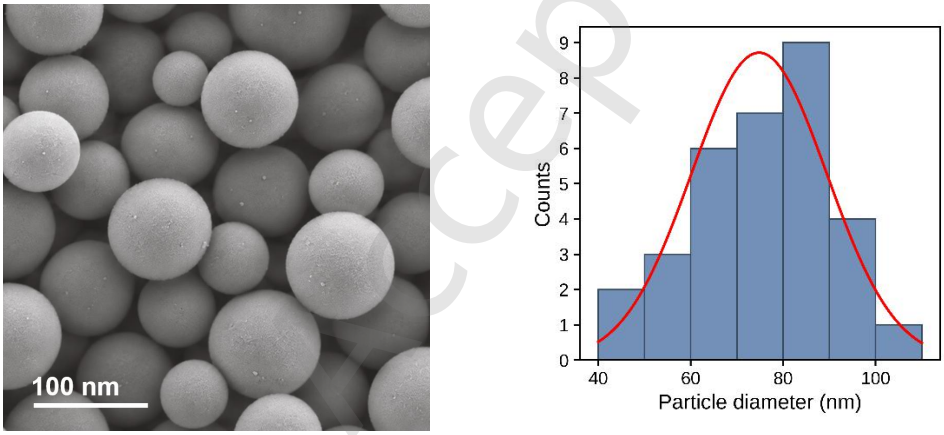


Figure S20. SEM image and corresponding particle-size distribution of the SiO_2 particles.

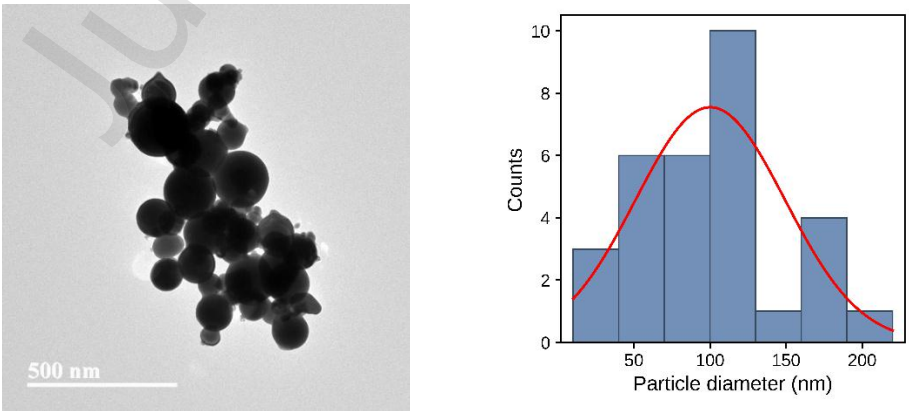


Figure S21. TEM image and corresponding particle-size distribution of the large Au particles.

Just Accepted

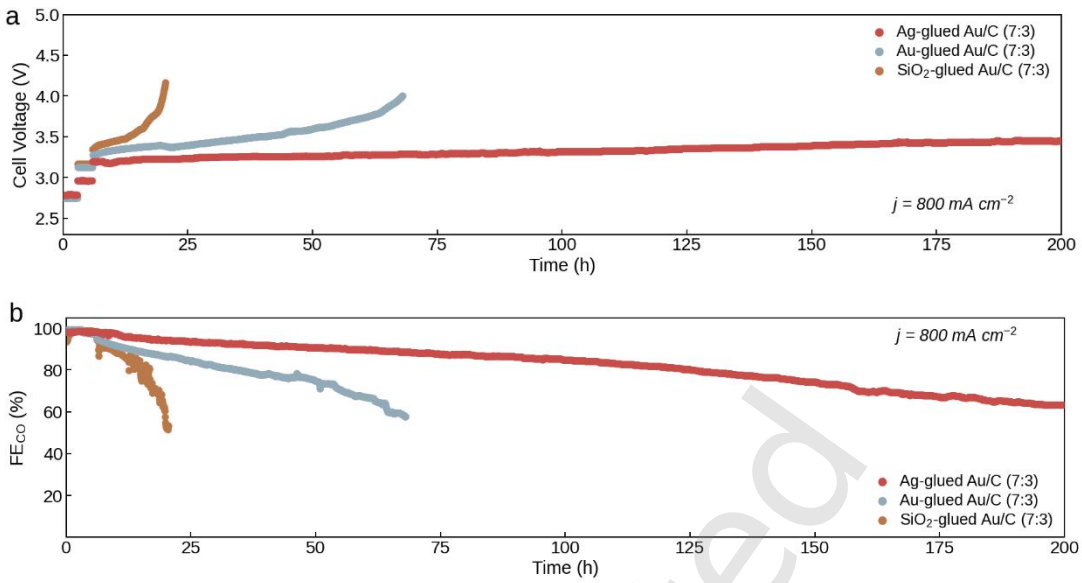


Figure S22. Zero-gap durability of Ag-glued Au/C (7:3), Au-glued Au/C (7:3) and SiO_2-glued Au/C (7:3) at 800 mA cm^{-2}. In all three catalysts the embedded phase is a large-particle component dispersed in the same nano-Au/C matrix: commercial Ag nanoparticles for Ag-glued Au/C, large Au nanoparticles for Au-glued Au/C, and large SiO_2 spheres for SiO_2-glued Au/C, with their morphologies and size ranges shown in Fig. S2, Fig. S21 and Fig. S20, respectively. (a) Cell voltage and (b) FE_{CO} as a function of operation time.

Text S9. Flow-rate-modulated operando EIS and DRT analysis.

Operando EIS was recorded on zero-gap MEAs with Ag-glued Au/C (7:3), Au-glued Au/C (7:3) or Au/C cathodes under galvanostatic control at 800 mA cm^{-2}. The cathode CO_2 flow rate was stepped as 1000 → 1500 → 2000 → 2500 → 3000 → 2500 → 2000 → 1500 → 1000 sccm, with each step held for 30 min (270 min in total); all other conditions followed Text S4. Spectra were acquired over 0.01 Hz to 100 kHz with an amplitude of 10% of the applied DC current and collected repeatedly within each step. DRT analysis was performed by Tikhonov regularization.

Relaxation features are resolved near 10^4 Hz, near 10^2 Hz, between ca. 3×10^2 and 3×10^3 Hz, and near 10^{-2} Hz. The features near 10^2 Hz and 10^{-2} Hz respond most strongly to the CO_2 feed rate and are therefore attributed to processes coupled to gas-phase transport, local CO_2 availability and liquid removal, whereas the feature near 10^4 Hz changes only weakly. The reversibility of these features upon returning to 1000 sccm is used as the main comparative indicator between the three catalyst layers. This flow-rate sensitivity is consistent with reports that the CO selectivity of gas-fed Ag-based electrodes is governed by the CO_2 supply rate relative to the applied current [36]. Because these measurements were performed under a different operating history and frequency range from the 60 h spectra in Fig. 5f, peak positions are compared only within this dataset. As DRT features arising from partially overlapping processes cannot be assigned uniquely, the analysis is used to compare the relative magnitude and reversibility of the flow-sensitive response between the two catalyst layers rather than to extract absolute transport parameters.

Just Accepted

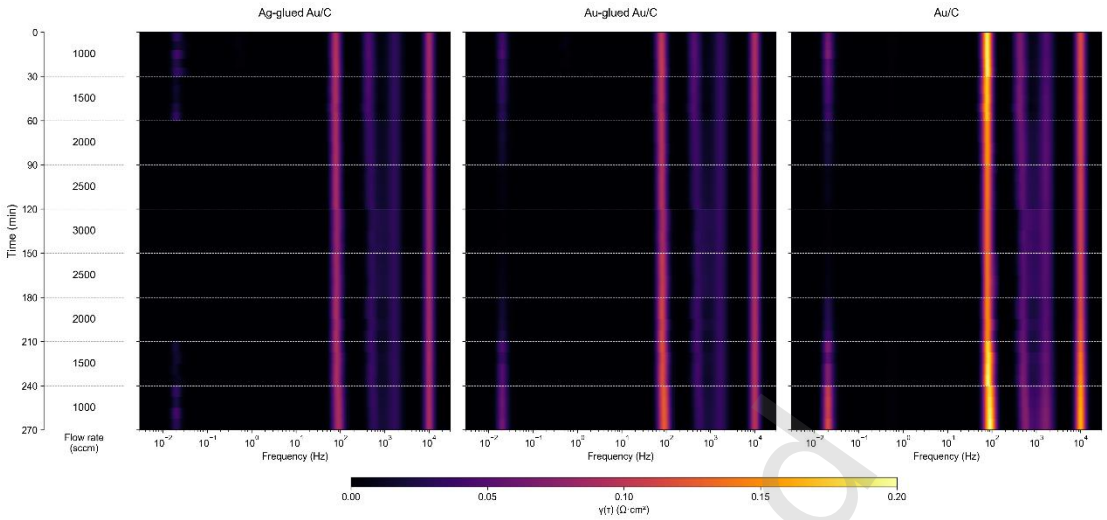


Figure S23. Flow-rate-modulated operando DRT maps of (left) Ag-glued Au/C, (middle) Au-glued Au/C and (right) Au/C in zero-gap electrolyzers at 800 mA cm^{-2}. $\gamma(\tau)$ is plotted against characteristic frequency and elapsed time; the cathode CO_2 flow rate was stepped as indicated on the left axis.

Just Accepted

Table S5. Comparison with representative state-of-the-art CO_2-to-CO electrolyzers

Reference	Catalyst / cathode	Electrolyzer type	Active area	High-rate performance	Stability condition	CO selectivity / FE_{CO} metric	Main comparison point
Dinh et al., 2018[S1]	Carbonate-derived Ag/PTFE composite electrode	Gas-fed flow cell / GDE	N.R.	>150 mA cm^{-2}	>100 h at >150 mA cm^{-2}	FE_{CO} >90%	Early high-rate Ag-based CO_2-to-CO benchmark with good stability, but not a zero-gap MEA system.
Endrődi et al., 2020[S2]	Ag cathode with PiperION membrane	Zero-gap CO_2 electrolyzer	N.R.	jCO >1.0 A cm^{-2}	N.R.	FE_{CO} up to 90%; CO_2 conversion 20–45%	Excellent high-current zero-gap performance, but long-term durability was not the central focus.
Endrődi et al., 2021[S3]	Ag-based cathode with operando alkali-cation activation	Water-fed zero-gap CO_2 electrolyzer	100 cm^2	jCO = 420 ± 50 mA cm^{-2}	>200 h at jCO = 420 ± 50 mA cm^{-2}	CO production rate maintained by periodic activation/regeneration	Strong water-fed zero-gap durability benchmark, relying on operando cation activation/regeneration.
Du et al., 2024[S4]	Ionomer-confined Ag GDE	MEA electrolyzer	4 cm^2	FE_{CO} >90% up to 600 mA cm^{-2}	>220 h at 300 mA cm^{-2}	FE_{CO} maintained above 75% during stability test	Ionomer pre-confinement improves mass transfer and stability, but stable current density is lower than this work.
Ko et al., 2024[S5]	Hydrophobicity-controlled Ag nanoparticles	Zero-gap CO_2 electrolyzer	10 cm^2	jCO = 298.39 mA cm^{-2} at 3.4 V	100 h at 150 mA cm^{-2}; 50 h at 3.4 V	FE_{CO} >90%; >95% during 150 mA cm^{-2} stability test	Hydrophobic Ag-NP design suppresses flooding, but active area and stable current density are lower.
Petrov et al., 2024[S6]	Ag cathode with perforated BPM architecture	Forward-bias BPM zero-gap electrolyzer	N.R.	FE_{CO} = 96% at 200 mA cm^{-2}	200 h at 100 mA cm^{-2}	EE_CO = 39%; FE_{CO} = 96% at 200 mA cm^{-2}	Stable BPM-based CO_2 electrolysis with reduced crossover, but long-term test was at lower current density.
Li et al., 2025[S7]	Ionomer-encapsulated Ag/C	10 cm × 10 cm MEA electrolyzer	100 cm^2	300 mA cm^{-2}	>60 h at 300 mA cm^{-2}	DOE-based optimization of FE_{CO} retention and operating conditions	Large-area MEA evaluation with optimized tri-phase interface, but current density is lower than this work.
Hao et al., 2025[S8]	Ag catalyst with acid-humidified CO_2 input	Scaled MEA electrolyzer	100 cm^2	100 mA cm^{-2}	4500 h at 100 mA cm^{-2}	FE_{CO} not compromised during long-term operation	Outstanding salt-management durability benchmark, but operated at much lower current density.
This work	**Ag-glued Au/C (7:3)**	**Zero-gap MEA electrolyzer**	**100 cm^2**	**800 mA cm^{-2}**	**200 h at 800 mA cm^{-2}**	**FE_{CO} decay rate = 0.122% h^{-1}; voltage decay rate = 1.3 mV h^{-1}**	**Combines large active area, industrial current density, and 200 h durability under zero-gap operation.**

Note: N.R. = not reported or not readily extractable from the accessible main text/abstract. FE_{CO} = Faradaic efficiency for CO; jCO = CO partial current density; EE_CO = energy efficiency for CO

Just Accepted

References for Supporting Information

[S1] Dinh, C.-T.; de Arquer, F. P. G.; Sinton, D.; Sargent, E. H. High rate, selective, and stable electroreduction of CO_2 to CO in basic and neutral media. ACS Energy Lett. 2018, 3, 2835–2840.

[S2] Endrődi, B.; Kecsenovity, E.; Samu, A.; Halmágyi, T.; Rojas-Carbonell, S.; Wang, L.; Yan, Y.; Janáky, C. High carbonate ion conductance of a robust PiperION membrane allows industrial current density and conversion in a zero-gap carbon dioxide electrolyzer cell. Energy Environ. Sci. 2020, 13, 4098–4105.

[S3] Endrődi, B.; Samu, A.; Kecsenovity, E.; Halmágyi, T.; Sebők, D.; Janáky, C. Operando cathode activation with alkali metal cations for high current density operation of water-fed zero-gap carbon dioxide electrolysers. Nat. Energy 2021, 6, 439–448.

[S4] Du, X. W.; Zhang, P.; Zhang, G.; Gao, H.; Zhang, L. L.; Zhang, M. M.; Wang, T.; Gong, J. L. Confinement of ionomer for electrocatalytic CO_2 reduction reaction via efficient mass transfer pathways. Natl. Sci. Rev. 2024, 11, nwad149.

[S5] Ko, Y. J.; Lim, C.; Jin, J.; Kim, M. G.; Lee, J. Y.; Seong, T. Y.; Lee, K. Y.; Min, B. K.; Choi, J. Y.; Noh, T.; Hwang, G. W.; Lee, W. H.; Oh, H. S. Extrinsic hydrophobicity-controlled silver nanoparticles as efficient and stable catalysts for CO_2 electrolysis. Nat. Commun. 2024, 15, 3356.

[S6] Petrov, K. V.; Koopman, C. I.; Subramanian, S.; Koper, M. T. M.; Burdyny, T.; Vermaas, D. A. Bipolar membranes for intrinsically stable and scalable CO_2 electrolysis. Nat. Energy 2024, 9, 932–938.

[S7] Li, M.; Yang, W.; Wang, S.; Zhao, W.; Hu, S. Tri-phase interface regulation of ionomer-encapsulated Ag/C catalyst for industrial CO_2 electrolyzer: A DOE-based analysis. Nano Res. 2025, 18, 94907611.

[S8] Hao, S.; Elgazzar, A.; Zhang, S. K.; Wi, T. U.; Chen, F. Y.; Feng, Y.; Zhu, P.; Wang, H. Acid-humidified CO_2 gas input for stable electrochemical CO_2 reduction reaction. Science 2025, 388, eadr3834.

Just Accepted